Neuron

Article

Dynamics of a disinhibitory prefrontal microcircuit in controlling social competition

Graphical abstract

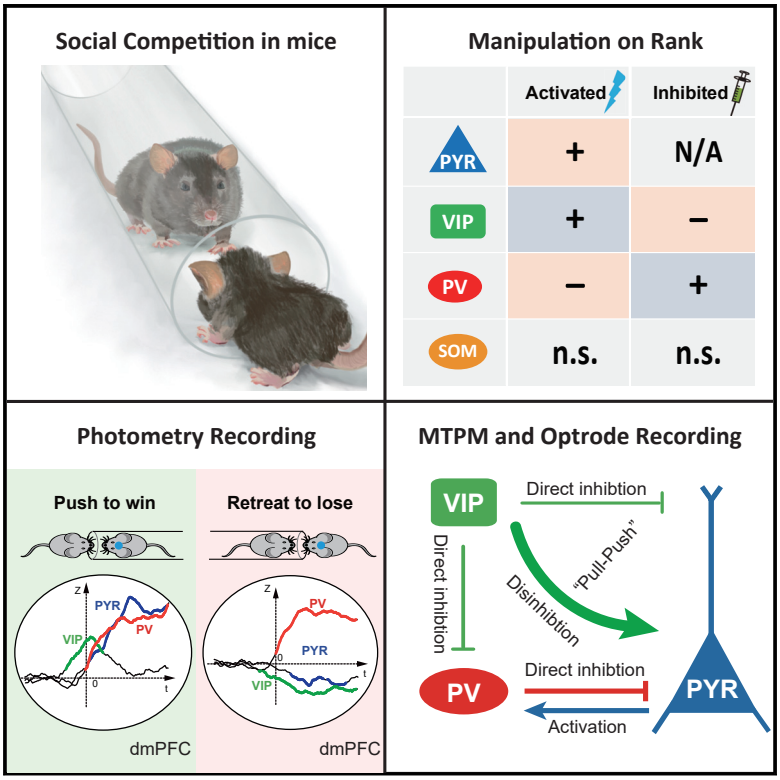

Highlights

- Activation of VIP or inhibition of PV interneurons in dmPFC induces winning
- Inhibition of VIP or activation of PV interneurons in dmPFC induces losing
- Calcium activities of dmPFC VIP neurons lead those of PYR and PV neurons in winning
- MTPM and optrode recordings reveal a disinhibitory VIP-PV-PYR microcircuit in dmPFC

Authors

Chaoyi Zhang, Hong Zhu, Zheyi Ni, ..., Jue Zhang, Heping Cheng, Hailan Hu

Correspondence

hong.zhu@emory.edu (H.Z.), huhailan@zju.edu.cn (H.H.)

In brief

How the dorsomedial prefrontal cortex (dmPFC) computes complex information in social competition within its local network is unclear. Here, Zhang et al. reveal a dynamic disinhibitory microcircuit, involving dmPFC VIP+, PV+, and pyramidal neurons, that controls social competition in the dominance tube test.

Zhang et al., 2022, Neuron *110*, 1–16
February 2, 2022
https://doi.org/10.1016/j.neuron.2021.10.034

CellPress

Please cite this article in press as: Zhang et al., Dynamics of a disinhibitory prefrontal microcircuit in controlling social competition, Neuron (2021), https://doi.org/10.1016/j.neuron.2021.10.034

Neuron

CellPress

Article

Dynamics of a disinhibitory prefrontal microcircuit in controlling social competition

Chaoyi Zhang,[1,2,10] Hong Zhu,[1,2,10,*] Zheyi Ni,[1,2,10] Qiuhong Xin,[1,2] Tingting Zhou,[1,2] Runlong Wu,[3] Guangping Gao,[4] Zhihua Gao,[2] Huan Ma,[2] Haohong Li,[2] Miao He,[5] Jue Zhang,[3] Heping Cheng,[3] and Hailan Hu[1,2,6,7,8,9,11,*]

[1]Department of Psychiatry of First Affiliated Hospital, Zhejiang University School of Medicine, Hangzhou 310058, China
[2]Liangzhu Laboratory, The MOE Frontier Research Center of Brain & Brain-Machine Integration, Zhejiang University School of Brain Science and Brain Medicine, 1369 West Wenyi Road, Hangzhou 311121, China
[3]Research Unit of Mitochondria in Brain Diseases, Chinese Academy of Medical Sciences, PKU–Nanjing Institute of Translational Medicine, Nanjing 211500, China
[4]Horae Gene Therapy Center, University of Massachusetts Medical School, Worcester, MA, USA
[5]Institutes of Brain Science, Department of Neurology, State Key Laboratory of Medical Neurobiology and MOE Frontiers Center for Brain Science, Fudan University, Shanghai, China
[6]Center for Brian Science and Brain-Inspired Intelligence, Guangdong-Hong Kong-Macao Greater Bay Area, Guangzhou 510515, China
[7]Research Units of Brain Mechanisms Underlying Emotion and Emotion Disorders, Chinese Academy of Medical Sciences, Beijing, 100730, China
[8]Key Laboratory for Biomedical Engineering of Ministry of Education, Zhejiang University, Hangzhou 310058, China
[9]Chuanqi Research and Development Center of Zhejiang University, Hangzhou 310058, China
[10]These authors contributed equally
[11]Lead contact
*Correspondence: hong.zhu@emory.edu (H.Z.), huhailan@zju.edu.cn (H.H.)
https://doi.org/10.1016/j.neuron.2021.10.034

SUMMARY

Social competition plays a pivotal role in determining individuals' social status. While the dorsomedial prefrontal cortex (dmPFC) is essential in regulating social competition, it remains unclear how information is processed within its local networks. Here, by applying optogenetic and chemogenetic manipulations in a dominance tube test, we reveal that, in accordance with pyramidal (PYR) neuron activation, excitation of the vasoactive intestinal polypeptide (VIP) or inhibition of the parvalbumin (PV) interneurons induces winning. The winning behavior is associated with sequential calcium activities initiated by VIP and followed by PYR and PV neurons. Using miniature two-photon microscopic (MTPM) and optrode recordings in awake mice, we show that VIP stimulation directly leads to a two-phased activity pattern of both PYR and PV neurons—rapid suppression followed by activation. The delayed activation of PV implies an embedded feedback tuning. This disinhibitory VIP-PV-PYR motif forms the core of a dmPFC microcircuit to control social competition.

INTRODUCTION

The health and quality of life of animals strongly depends on their dominance status, which is acquired through repeated social competitions (Sandi and Haller, 2015; Sapolsky, 2005; So et al., 2015; Wilson, 2000). The outcome of social competition is often not just a matter of body size or physical strength (Mooney et al., 2014), but rather is determined by personality traits that are regulated by high cortical functions (Fernald, 2014; Zhou et al., 2018). Among the high cortical areas, the medial prefrontal cortex (mPFC) has been particularly implicated in social dominance (Rushworth et al., 2013; Wang et al., 2014). The mPFC encodes several cognitive features that may be related to social competition, such as effort-based decision making (Bailey et al., 2016; Friedman et al., 2015; Holroyd and McClure, 2015; Walton et al., 2002) and action planning in challenging or competitive situations (Fujii et al., 2009; Hillman and Bilkey, 2012; Hosokawa and Watanabe, 2012; Porter et al., 2019; Warden et al., 2012). A lesion in the prefrontal cortex (PFC) in rodents or primates impairs processing of social hierarchy information, reduces social interest, and lowers social rank (Blair and Cipolotti, 2000; Mah et al., 2004; Rudebeck et al., 2006, 2007).

In mice, social dominance can be measured by the tube test, where two mice compete for passage in a narrow tube (Fan et al., 2019; Lindzey et al., 1961; Wang et al., 2011). In the tube test competition, manipulation of the synaptic strength or activity of the dorsalmedial prefrontal cortex (dmPFC) neurons bidirectionally controls the outcome of competition and dominance status of mice (Wang et al., 2011; Zhu and Hu, 2018). While the upstream input to the dmPFC has been mapped in win- or defeat-related behavior (Franklin et al., 2017; Nelson et al., 2019; Zhou et al., 2017), little is known about how information

Please cite this article in press as: Zhang et al., Dynamics of a disinhibitory prefrontal microcircuit in controlling social competition, Neuron (2021), https://doi.org/10.1016/j.neuron.2021.10.034

is processed and computed within the mPFC local microcircuits during social competition.

PFC function is known to depend on a delicate balance between excitation and inhibition, mediated by the excitatory pyramidal (PYR) neurons and a variety of GABAergic interneurons (Kamigaki and Dan, 2017; Kvitsiani et al., 2013; Pi et al., 2013). A majority (~80%) of cortical interneurons are the vasoactive intestinal polypeptide (VIP), parvalbumin (PV), and somatostatin (SOM) neurons (Kepecs and Fishell, 2014; Rudy et al., 2011). These distinct types of interneurons are differentially modulated by sensory stimuli or motor behaviors (Fu et al., 2014; Hattori et al., 2017; Kerlin et al., 2010) as well as brain states and neuromodulatory inputs (Alitto and Dan, 2013; Zhang et al., 2014). Thus, different interneuron types may play diverse roles in local computation and exert distinct control on the excitatory output (Huang, 2014; Kepecs and Fishell, 2014). Recently, a series of elegant work has established the role of mPFC interneurons in various social behaviors, including social interaction (Bicks et al., 2020; Cao et al., 2018; Yizhar et al., 2011), conditioned social fear (Xu et al., 2019), representation of conspecific sex (Kingsbury et al., 2020), and affective state discrimination (Scheggia et al., 2020). However, it has remained unexplored how different mPFC cell types engage in social competition, what their dynamics are like, and how they regulate the dominance behavior.

To address these questions, we set out to apply cell-type-specific optogenetic and chemogenetic tools to manipulate the activity of PYR neurons and three major interneuron types in the dmPFC during social competition. We found that activation or inhibition of these neurons led to distinct, or even opposite, outcomes in dominance tube test performance. Cell-type-specific calcium imaging, optrode, and miniature two-photon microscope (MTPM) recordings further revealed dynamic interactions among these cell types and identified a potential disinhibitory microcircuit from VIP to PYR via PV neurons in social competition.

RESULTS

Behavioral effects of activating different dmPFC neuron types in the tube test

We previously found that photostimulation of dmPFC neurons and, in particular, the excitatory PYR neurons induces winning behaviors in the dominance tube test (Figures 1A–1D) (Zhou et al., 2017). In order to systemically examine the contribution of different dmPFC interneuron types to social competition, we employed three Cre mouse lines (SOM-Cre, PV-Cre, and VIP-Cre; Taniguchi et al., 2011) to drive interneuron-type-specific expression of ChR2 (Boyden et al., 2005) (Figures 1E–1O). Injection of adeno-associated virus (AAV) encoding Cre-dependent ChR2 into the bilateral dmPFC of the three Cre lines or crossing these lines with a Cre-dependent ChR2 mouse line Ai32 (Madisen et al., 2012) allowed specific optogenetic activation of different interneuron types in the dmPFC (Figures 1E, 1H, 1L, and S1A–S1C). While activation of SOM neurons in the dmPFC caused an insignificant change in tube test rank (Figures 1E–1G), photoactivation of PV neurons led to a rank decline ($p = 0.004$, two-way ANOVA; Figures 1I and 1J). Detailed video analysis revealed that these rank-declined mice showed significantly decreased effortful behaviors including push and resistance, and increased retreats (Mann-Whitney U test; Figure 1K). In contrast, photostimulation of VIP neurons successfully induced rank elevation ($p = 0.037$, two-way ANOVA; Figures 1M and 1N). There was significantly more pushes and there were fewer retreats in these rank-elevated mice (Mann-Whitney U test; Figure 1O). General locomotion was not affected under either PV or VIP stimulation (Figures S2). As a control, dmPFC photostimulation of PV::EYFP and VIP::EYFP mice did not induce any rank change (Figures 1J and 1N).

Behavioral effects of inhibiting different dmPFC interneurons in the tube test

We next examined the necessity of different dmPFC interneuron types in tube test competition (Figure 2). We applied the inhibitory DREADD (designer receptors exclusively activated by designer drugs) system (Armbruster et al., 2007) by bilaterally injecting AAV encoding Cre-dependent Gi-coupled hM4D receptor into the dmPFC of SOM-Cre (Figures 2B and S3A), PV-Cre (Figures 2E and S3B), or VIP-Cre (Figures 2I and S3C) mice. One mouse from the four-mouse groups with stable ranks was intraperitoneally injected with Clozapine-N-oxide (CNO) and the other three mice were injected with saline as a control (Figure 2A). Consistent with the activation result, application of CNO in SOM::hM4D mice did not cause any significant rank change in the tube test (Figures 2C and 2D). In PV::hM4D mice, however, we observed five of seven mice with elevated ranks starting at 0.5 h after CNO injection ($p = 0.007$, two-way ANOVA; Figures 2F and 2G). Detailed video analysis revealed that these rank-elevated mice showed more pushes and resistance and fewer retreats (Mann-Whitney U test; Figure 2H). In contrast, chemogenetic inhibition of dmPFC VIP neurons induced a rank drop in five of eight mice ($p < 0.001$, two-way ANOVA; Figures 2J and 2K), and there was a significant decrease in pushes and resistance and an increase in retreat behaviors in these rank-declined mice (Mann-Whitney U test; Figure 2L). As a control for drug effect, saline injection caused no significant rank change in PV::hM4D and VIP::hM4D mice (Figures 2G and 2K). As a control for viral effect, CNO injection in PV::EYFP and VIP::EYFP mice caused no significant rank change (Figures 2G and 2K).

dmPFC neurons are activated during effortful pushes and inhibited during passive retreats in the dominance tube test

We next wished to observe the real-time activity of different dmPFC neuronal types when mice compete in the tube test. Using the fiber photometry system (Flusberg et al., 2005; Gunaydin et al., 2014) in the dmPFC (Figure 3A), we first monitored the overall dmPFC activity by expressing genetically encoded Ca^{2+} indicator GCaMP6s (Chen et al., 2013) under the human synapsin promoter in the right dmPFC and implanting an optic fiber 300 μm above the injection site (Figure 3B). To align the behavior, we used an elongated tube with two doors close to the entries, which open 5 s after the arrival of both mice (Figure 3C). Either winning or losing mice from mouse pairs with stable ranks were recorded for their dmPFC photometry signals, while their

Please cite this article in press as: Zhang et al., Dynamics of a disinhibitory prefrontal microcircuit in controlling social competition, Neuron (2021), https://doi.org/10.1016/j.neuron.2021.10.034

CellPress

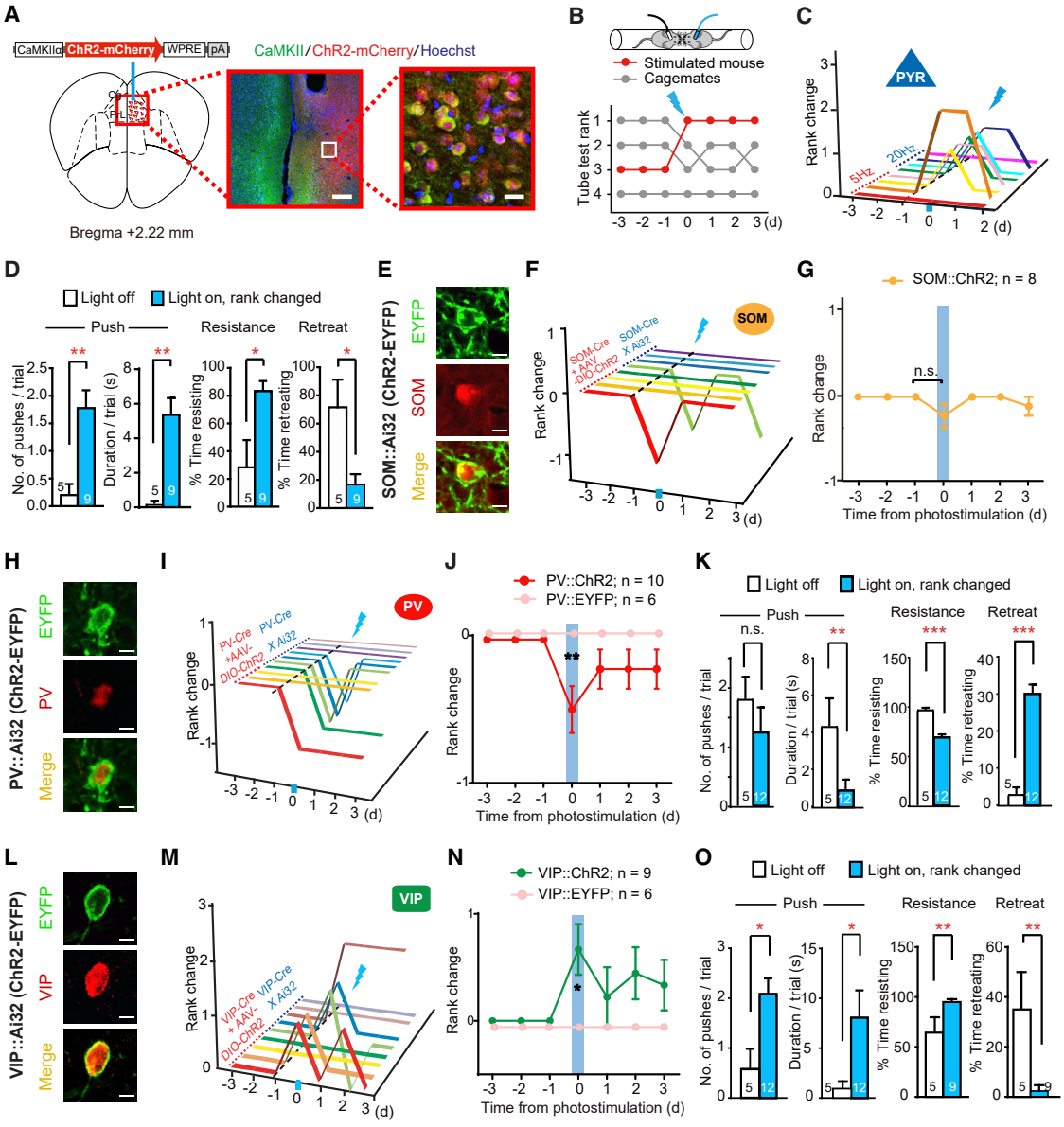

Figure 1. Behavioral effects of optogenetic activation of different dmPFC neuron types in the tube test

(A) On the left, the schematic illustrates the CaMKIIα::ChR2 viral construct and viral injection site in the dmPFC (including the prelimbic (PrL) region and anterior part of the cingulate (Cg) cortex). On the right, fluorescence images show immunostained CaMKII with expression of ChR2-mCherry. Green, CaMKII; red, ChR2-mCherry; and blue, Hoechst. Scale bars, 200 μm (middle) and 20 μm (right).

(B) Daily tube test results of a cage of four mice injected with CaMKIIα::ChR2 virus before and after acute dmPFC photostimulation of the rank-3 mouse on day 0.

(C) Summary of rank change in the tube test after photostimulation of PYR neurons. Each line represents one animal.

(D) Behavioral performance of the same CaMKIIα::ChR2 mice with or without photoactivation. The number of trials is indicated in each bar. Only mice showing rank changes are analyzed. Mann-Whitney U test.

(E, H, and L) Fluorescence images show immunostained SOM (E), PV (H), or VIP (L) neurons in SOM-Cre::Ai32 (E), PV-Cre::Ai32 (H), or VIP-Cre::Ai32 (L) mice, confirming the specificity of ChR2-EYFP expression in corresponding cell types. Scale bars, 10 μm.

(F, I, and M) Rank change in the tube test after photostimulation of SOM (F), PV (I), or VIP neurons (M). Each line represents one animal. Light stimulation was delivered during the tube test on day 0.

(G) Average rank change in daily tube test after optogenetic activation of SOM neurons in dmPFC. Wilcoxon matched-pairs signed-rank test.

(J and N) Photoactivation of PV neurons induces ranking decline (J), whereas photoactivation of VIP neurons induces ranking elevation (N). Two-way repeated-measure ANOVA, Bonferroni multiple comparisons post hoc tests.

(K and O) Behavioral performance of the same PV::ChR2 (K) and VIP::ChR2 (O) mice with or without photoactivation. The number of trials is indicated in each bar. Only mice showing rank changes are analyzed. Mann-Whitney U test.

Error bars indicate ± SEM. *p < 0.05; **p < 0.01; ***p < 0.001; n.s., not significant. See also Figures S1 and S2.

Please cite this article in press as: Zhang et al., Dynamics of a disinhibitory prefrontal microcircuit in controlling social competition, Neuron (2021), https://doi.org/10.1016/j.neuron.2021.10.034

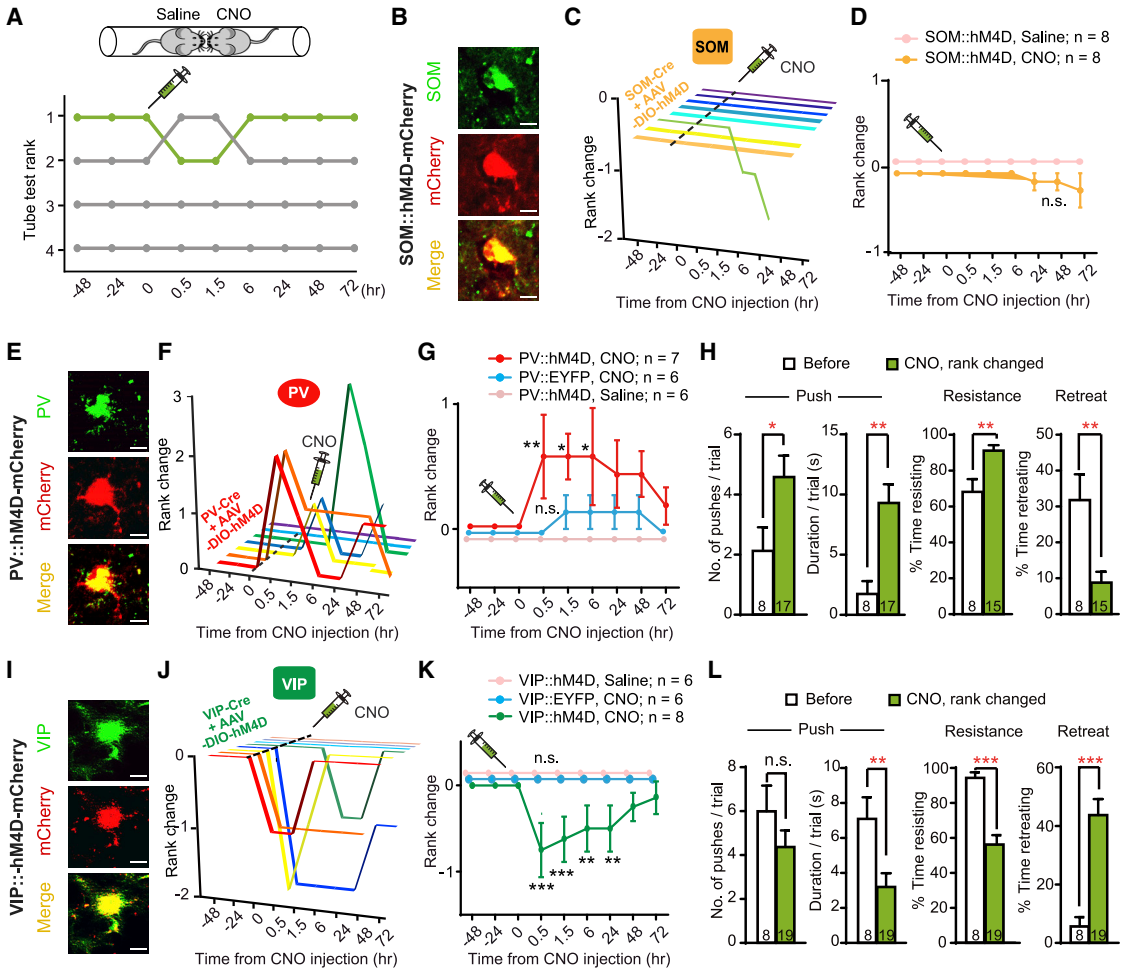

Figure 2. Behavioral effects of chemogenetic inhibition of different dmPFC interneurons in the tube test

(A) Tube test results for a cage of VIP::hM4D-expressing mice before and after intraperitoneal injection of CNO into the rank-1 mouse at time 0.

(B, E, and I) Immunostaining confirming the specificity of hM4D expression in SOM-Cre (B), PV-Cre (E) or VIP-Cre (I) mice. Scale bars, 10 μm.

(C, F, and J) Summary of rank change in the tube test after chemogenetic inhibition of SOM (C), PV (F), and VIP (J) neurons. Each line represents one animal.

(D, G, and K) Average rank change after CNO or saline injection of SOM::hM4D (D), PV::hM4D (G), or VIP::hM4D (K) mice. Two-way repeated-measure ANOVA; Bonferroni multiple comparisons post hoc tests.

(H and L) Behavioral performance of the same PV::hM4D (H) and VIP::hM4D (L) mice before and after CNO injection. The number of trials is indicated in each bar. Only mice showing rank changes are analyzed. Mann-Whitney U test.

Error bars indicate ± SEM. *p < 0.05; **p < 0.01; ***p < 0.001; n.s., not significant. See also Figure S3.

behaviors were videotaped and annotated into push and retreat epochs (Figure 3C). Three to four weeks after viral injection, mice were acclimated to walk through the tube with or without an opponent on the other side. No significant change in GCaMP6s fluorescence signal was detected when mice walked through the tube without an opponent ($p > 0.05$, permutation test, n = 58 trials from six mice; Figures 3D and 3E) or when GFP-expressing mice engaged in the tube test ($p > 0.05$, permutation test, n = 26 trials from two mice; Figures 3F and 3G). However, when test mice had direct confrontation with an opponent, the dmPFC Ca^{2+} signal increased immediately after the recorded mice initiated pushes that led to winning. The average signal peak (*Z* score) was 4.0 ± 0.7 (mean ± SEM, $p < 0.05$, permutation test, n = 55 trials from seven mice; Figures 3H and 3J). In contrast, a slight but significant decrease in dmPFC Ca^{2+} signal was observed from retreats that led to loss. The average signal trough (*Z* score) was −1.8 ± 0.6 (mean ± SEM, $p < 0.05$, permutation test, n = 42 trials from seven mice; Figures 3I and 3J). This Ca^{2+} dynamic suggests that dmPFC neurons were generally activated during "effortful" pushes and inhibited during "passive" retreats in social competitions.

Different dmPFC neuron types are differentially recruited during effortful pushes and passive retreats in the dominance tube test

To better understand how different neuron types in the dmPFC microcircuits react during social competitions, we separately performed fiber photometry Ca^{2+} recording on the PYR, PV,

Please cite this article in press as: Zhang et al., Dynamics of a disinhibitory prefrontal microcircuit in controlling social competition, Neuron (2021), https://doi.org/10.1016/j.neuron.2021.10.034

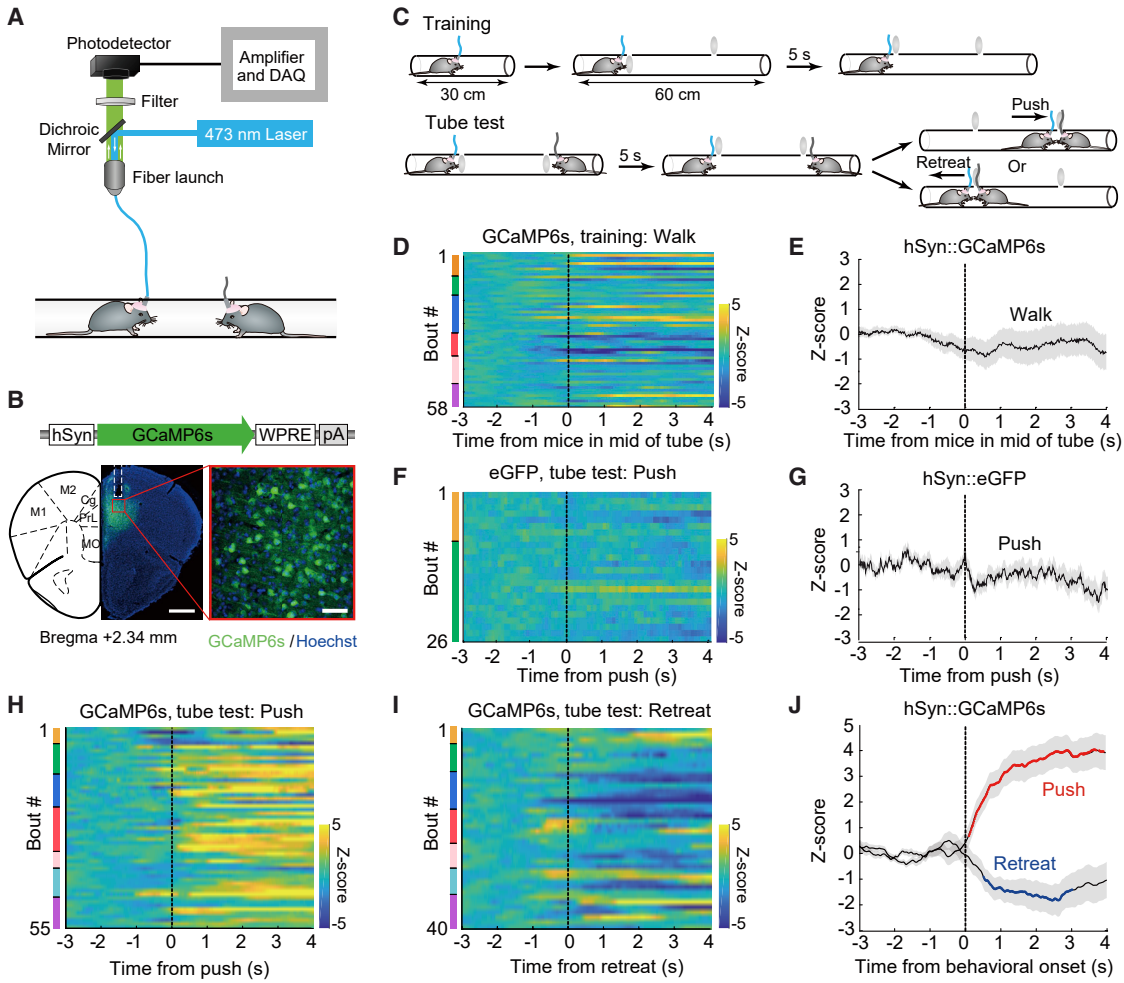

Figure 3. Ca^{2+} activity of dmPFC neurons during pushes and retreats in the tube test

(A) Schematic illustrating the fiber photometry setup.

(B) Schematic illustrating the hSyn::GCaMP6s viral construct, injection site, and optic fiber placement. Scale bars, 500 μm (left) and 50 μm (right).

(C) Illustration of modified tube test setup and procedures of training (top) and tube test (bottom). See STAR Methods for details.

(D and E) Heatmap (D) and peri-event plot (E) of *Z*-scored dmPFC Ca^{2+} signals when mice walk through the tube. Signals are aligned to the time point when mice pass through the middle of the tube. In the heatmap, different color bars on the left represent different mice. n = 58 trials from six mice.

(F and G) Heatmap (F) and peri-event plot (G) of *Z*-scored dmPFC Ca^{2+} signals during push in mice expressing the control eGFP virus. Signals are aligned to the time point when mice initiate pushes. n = 26 trials from two mice.

(H and I) Heatmap of *Z*-scored dmPFC Ca^{2+} signals aligned to the onset of pushes (H; n = 55 trials from seven mice) and retreats (I; n = 42 trials from seven mice).

(J) Peri-event plot of *Z*-scored dmPFC Ca^{2+} signals during push (red) and retreat (blue) epochs. Solid lines indicate mean and shaded areas indicate SEM. Colored line segments indicate statistically significant fluorescence increase or decrease from the baseline ($p < 0.05$; permutation test).

and VIP neurons in the dmPFC. We injected either AAV expressing GCaMP6s under the CaMKIIα promoter into the dmPFC of wild-type mice or AAV expressing Cre-inducible GCaMP6s into the dmPFC of PV-Cre or VIP-Cre mice, and we verified cell-type-specific expression with immunostaining (Figures S4A–S4F). Similar to the dmPFC whole network activity as shown above, PYR neurons were activated during the push epochs (*Z* score = 4.86 ± 1.34, mean ± SEM, $p < 0.05$, permutation test, n = 40 trials from five mice; Figures 4A and 4C) and inhibited during retreats (*Z* score = −1.48 ± 0.39, mean ± SEM, $p < 0.05$, permutation test, n = 39 trials from four mice; Figures 4B and 4C). VIP neurons showed a similar trend as PYR neurons, being activated during pushes (*Z* score = 2.45 ± 0.8, mean ± SEM, $p < 0.05$, permutation test, n = 34 trials from four mice; Figures 4D and 4F) and inhibited during retreats (*Z* score = −2.12 ± 0.33, mean ± SEM, $p < 0.05$, permutation test, n = 38 trials from six mice; Figures 4E and 4F), but with some difference in signal dynamics (see below). PV neurons, on the other hand, showed a significant increase in both push epochs (*Z* score = 4.56 ± 0.94, mean ± SEM, $p < 0.05$, permutation test, n = 41 trials from eight mice; Figures 4G and 4I) and retreat epochs (*Z* score = 3.62 ± 0.78, mean ± SEM, $p < 0.05$, permutation test, n = 37 trials from six mice; Figures 4H and 4I). Analysis of the latency of signal onset during push epochs revealed that Ca^{2+} signals of VIP neurons rose

Please cite this article in press as: Zhang et al., Dynamics of a disinhibitory prefrontal microcircuit in controlling social competition, Neuron (2021), https://doi.org/10.1016/j.neuron.2021.10.034

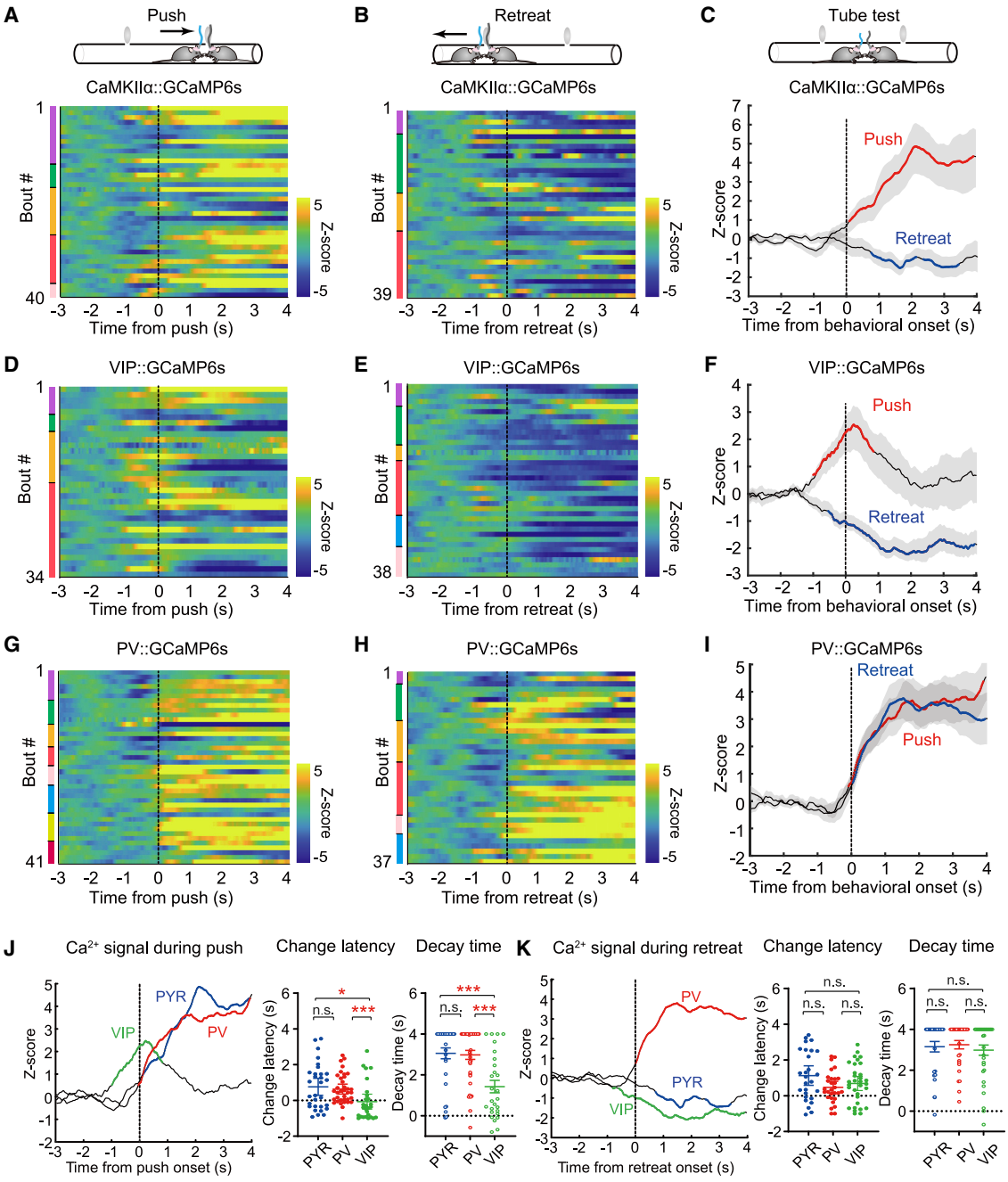

Figure 4. Differential activity dynamics of dmPFC neuronal types during pushes and retreats in the tube test

(A, D, and G) Heatmap of *Z*-scored Ca^{2+} signals from dmPFC PYR (A; n = 40 trials from five mice), VIP (D; n = 34 trials from four mice), and PV (G; n = 41 trials from eight mice) neurons aligned to the onset of push bouts. Color bars on the left represent different individual mice.

(B, E, and H) Heatmap of *Z*-scored Ca^{2+} signals from dmPFC PYR (B; n = 39 trials from four mice), VIP (E; n = 38 trials from six mice), and PV (H; n = 37 trials from six mice) neurons aligned to the onset of retreat bouts.

(C, F, and I) Peri-event plots of *Z*-scored Ca^{2+} signal changes from PYR (C), VIP (F), and PV (I) neurons during push (red) and retreat (blue) epochs. Solid lines indicate mean and shaded areas indicate SEM. Colored thick line segments indicate statistically significant fluorescence change from the baseline in push (red) and retreat (blue) epochs ($p < 0.05$; permutation test).

(J) Alignment of peri-event plots of *Z*-scored Ca^{2+} signal changes of PYR, PV, and VIP neurons during push epochs (left). Colored line segments indicate statistically significant fluorescence change from the baseline. Latency to significant change (middle) and decay time (right) of Ca^{2+} signals indicate different dynamics of distinct neuron types in response to push onset (see STAR Methods and Figure S5 for definition of change latency and decay time). Mann-Whitney U test.

(legend continued on next page)

Please cite this article in press as: Zhang et al., Dynamics of a disinhibitory prefrontal microcircuit in controlling social competition, Neuron (2021), https://doi.org/10.1016/j.neuron.2021.10.034

before the push onset, with a shorter latency than the rise of Ca^{2+} signals from PYR and PV neurons (VIP versus PYR, p = 0.04; VIP versus PV, p = 0.0004; Mann-Whitney U test; Figures 4J, S5A, and S5B), and were more transient (VIP versus PYR, p = 0.0002; VIP versus PV, p < 0.0001; Mann-Whitney U test; Figures 4J, S5D, and S5E). In retreat epochs, there was no obvious difference in change latency and decay time of Ca^{2+} signals among the three cell types (Figures 4K, S5C, and S5F). Collectively, the Ca^{2+} signals of the three neural types during competition were largely consistent with the prediction from the manipulation results, except for the increase of PV response during pushes. In addition, the difference in onset time suggests that VIP neurons may be responsible for initiating dmPFC microcircuit activity during push epochs.

Effects of inhibiting PV or VIP neurons on dmPFC network activity

Intrigued by the calcium dynamics of dmPFC VIP and PV neurons and in light of their opposing effects on social competition, we set out to explore how these two neuron types influence dmPFC network activity. We first tested the effects of silencing PV and VIP interneurons on dmPFC network activity *in vivo*, using optogenetics combined with the fast high-resolution miniature two-photon microscopy (FHIRM-TPM V2.0) system (Zong et al., 2017, 2021) (Figure 5A). We coexpressed in the dmPFC of PV-Cre or VIP-Cre transgenic mice two AAVs: one expressing GCaMP6f under the human synapsin promoter and the other expressing Cre-dependent inhibitory opsin JAWs (Chuong et al., 2014) (Figures 5A, 5B, and S6; STAR Methods). This allowed us to simultaneously track the calcium activity of dmPFC neurons in the field of view (FOV) at the single cell level while optogenetically inhibiting PV or VIP neurons in awake mice.

We first characterized the response dynamics of dmPFC neurons while optogenetically inhibiting PV neurons (Figures 5C–5G). Fluorescence colabeling revealed that 9% (15 of 169 neurons from three mice) of GCaMP6f-expressing neurons coexpressed JAWs-tdTomato, which were PV+ neurons (Figure 5C). Sixty percent of these (9 of 15) PV+ neurons were inhibited during the light-on session (e.g., neurons 1 and 2 in Figure 5D; Figures 5D–5F). Among the 154 non-PV dmPFC neurons, 16% were significantly excited and 4% were inhibited during the light-on session (Figures 5E and 5F). Overall, when PV neurons were inhibited, the network activity of dmPFC was significantly increased (see STAR Methods for calculation, p = 0.009, two-way ANOVA; Figures 5G, S7A, and S7B).

We then characterized the response dynamics of dmPFC neurons while optogenetically inhibiting VIP neurons (Figures 5H–5L). The results showed that 4.6% (6 of 129 from two mice) of GCaMP6f-expressing neurons coexpressed JAWs-tdTomato, which were VIP+ neurons (Figure 5H); 67% of these VIP+ neurons were inhibited during the light-on session (e.g., neurons 1 and 2 in Figure 5I; Figures 5I–5K). Among the remaining 123 non-VIP neurons, 13% showed significantly decreased calcium transients and 3% were activated during the light-on session (Figures 5J and 5K). Overall, during light stimulation when VIP neurons were inhibited, there was a decrease in the network activity of dmPFC (p = 0.003, two-way ANOVA; Figures 5L, S7C, and S7D). Collectively, these data confirmed an inhibitory role of PV and an excitatory role of VIP neurons in regulating general dmPFC network activity.

Effects of activating PV neurons on dmPFC neural network activity

In order to infer the sequence of activity of VIP, PYR, and PV neurons, we needed to examine their dynamics at even higher temporal resolution. For this, we made single-unit electrophysiological recordings of dmPFC neurons while optogenetically activating PV and VIP neurons in awake mice (Figures 6 and 7). We performed 16-channel optrode recording in the dmPFC layer V/VI of PV-Cre::Ai32 or VIP-Cre::Ai32 transgenic mice (Chen et al., 2017), while delivering blue light to stimulate PV or VIP interneurons (Figures 6A, 7A, and S8). We recorded 201 well-isolated neurons from five PV-Cre::Ai32 mice, including seven optogenetically tagged PV neurons (Figure 6B; see STAR Methods for criteria of optogenetic tagging), 139 wide-spike (WS) units (mostly putative PYR [pPYR] neurons), and 55 narrow-spike (NS) units (putative interneuron [pIN]) (trough-to-peak duration of 400 μs as the borderline for NS versus WS clarification; see STAR Methods for more criteria of single-unit isolation and cell-type classification) (Chen et al., 2017; Stark et al., 2013; Xu et al., 2019). Based on firing frequency, NS neurons can be further divided into 16 fast-spiking interneurons (FSIs; frequency ≥ 8 Hz), which are putative parvalbumin (pPV) neurons (Kim et al., 2016; Varga et al., 2012), and 39 NS non-FSIs (< 8Hz) (Figures 6C and 6D). For photostimulation of PV interneurons, we used the same constant pattern (constant 10 s) that successfully decreased the tube test rank (Figures 1I-1K and 6D). During PV photostimulation, the most striking change was a universal decrease in the activity of the majority (92%, 128 of 139) of WS pPYR neurons (Figures 6D and 6E). Many FSI (31%) and NS non-FSI (72%) neurons were also inhibited (Figures 6F and 6G), suggesting that PV neurons can inhibit each other or other types of interneurons.

Activation of VIP neurons leads to two-phased activity

For stimulation of VIP neurons, we first applied the 1-Hz light stimulation protocol to the VIP-Cre::Ai32 mice to tag the dmPFC VIP neurons and reveal the full dynamics of neural response after each pulse of VIP activation (Figures 7A–7H). We recorded 156 well-isolated neurons, including 4 optogenetically tagged VIP neurons (Figure 7B), 127 WS pPYR units, 14 NS non-FSI units, and 11 FSI pPV units (Figure 7C). Consistent with a previously reported study (Pi et al., 2013), neuronal responses can be categorized into inhibition (Inh), inhibition-activation (Inh-act), and

(K) Alignment of peri-event plots of *Z*-scored Ca^{2+} signal changes of PYR, PV, and VIP neurons during retreat epochs (left). Colored line segments indicate statistically significant fluorescence change from the baseline. Latency to significant change (middle) and decay time (right) of Ca^{2+} signals indicate similar dynamics of distinct neuron types in response to retreat onset. Mann-Whitney U test.
Error bars indicate ± SEM. *p < 0.05; ***p < 0.001; n.s., not significant. See also Figures S4, S5 and S12.

Please cite this article in press as: Zhang et al., Dynamics of a disinhibitory prefrontal microcircuit in controlling social competition, Neuron (2021), https://doi.org/10.1016/j.neuron.2021.10.034

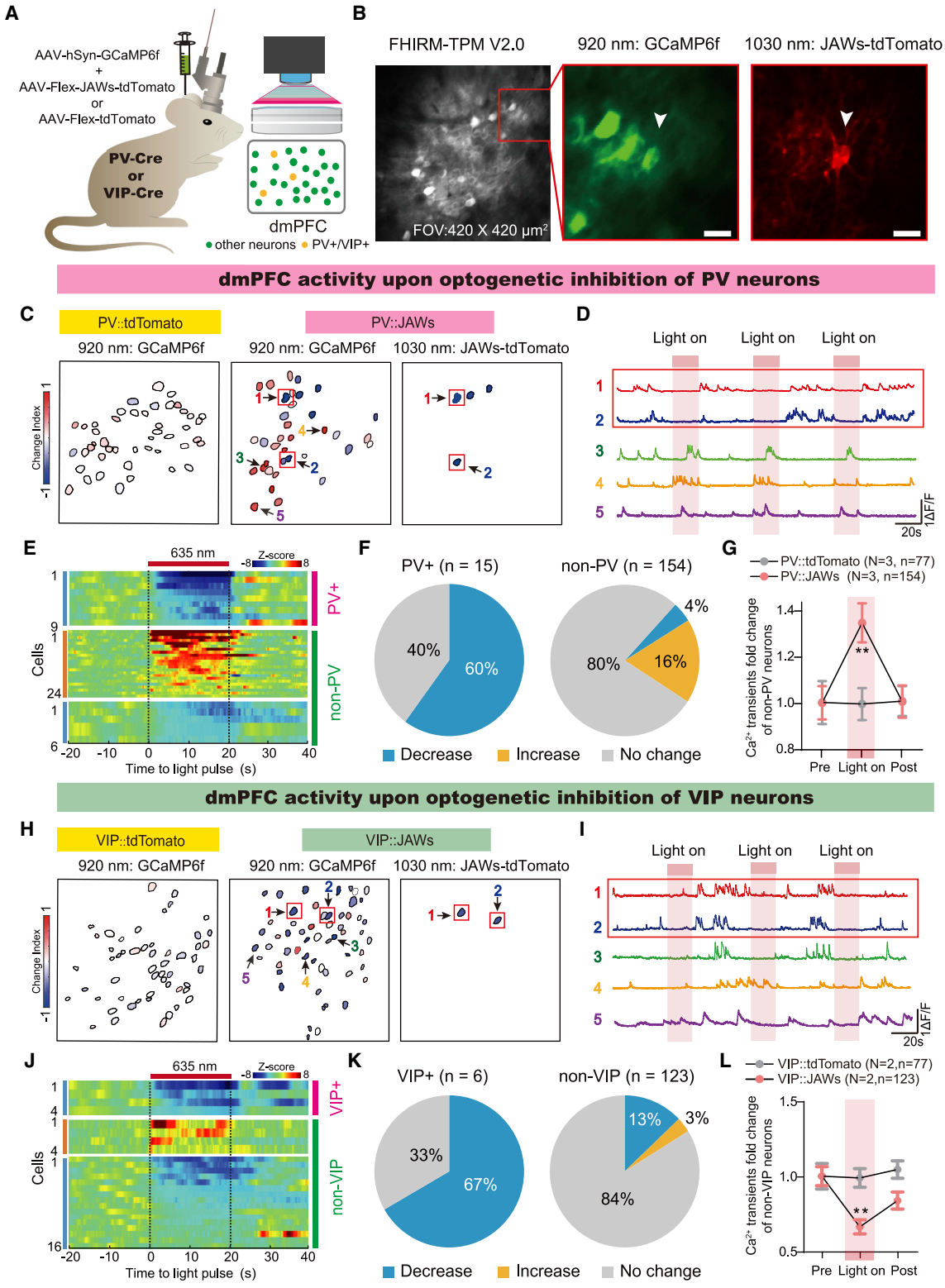

Figure 5. Effects of inhibiting PV or VIP neurons on dmPFC neural network activity

(A) Setup of fast high-resolution miniature two-photon microscopy version 2 (FHIRM-TPM V2.0) (Zong et al., 2021), combined with the GRIN lens in the dmPFC of awake, head-fixed mice (left), and diagram of dual-color imaging (right). See STAR Methods for details.

(legend continued on next page)

Please cite this article in press as: Zhang et al., Dynamics of a disinhibitory prefrontal microcircuit in controlling social competition, Neuron (2021), https://doi.org/10.1016/j.neuron.2021.10.034

CellPress

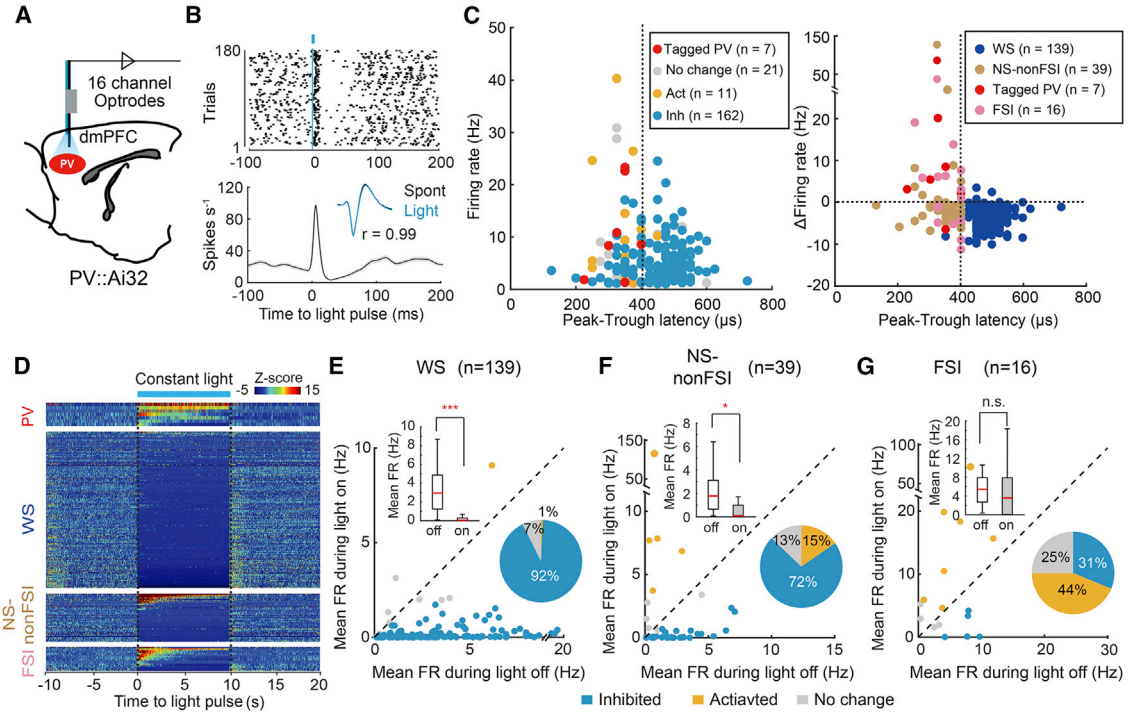

Figure 6. Effects of activating PV neurons on dmPFC neural network activity

(A) Schematic illustration of *in vivo* optrode recording in the dmPFC of PV-Cre::Ai32 mice.

(B) Raster plot (top) and peri-stimulus time histogram (PSTH, bottom) of a representative tagged PV neuron. In the inset, light-evoked spike waveforms (blue) were similar to spontaneous ones (black). Pearson's correlation, r = 0.99.

(C) On the left, baseline firing rate plotted against peak-to-trough latency of all recorded units. Colored circles indicate neurons that showed significant differences in firing rates during 10-s constant light on versus light off. Blue, inhibition; orange, activation; and gray, no change. On the right, light-induced firing rate changes plotted against peak-to-trough latency of all recorded units. Colors indicate different cell types. Blue, WS (wide-spike neuron); brown, NS non-FSI (narrow-spike non-fast-spiking interneuron); red, tagged PV; and pink, FSI (fast-spiking interneuron).

(D) PSTHs of all recorded neurons, including tagged PV cells and nontagged WS, NS non-FSI, and FSI cells, ranked by a descending order of firing rate during the 10-s constant light-on period.

(E–G) Scatterplots of the mean firing rates (FRs) of WS (E), NS non-FSI (F), and FSI (G) neurons during the 10-s constant light-on epoch, against firing rates during the 10-s light-off epoch. Colored circles indicate neurons that showed significant light-induced firing rate increase (orange) or decrease (blue). Inset pie graphs show the percentage of neurons that had significantly higher, lower, or unchanged firing rates during the light stimulation. Inset boxplots show the overall firing rate during the 10-s light-off and 10-s light-on epoch. Data in all figures are median ± 1.5× interquartile range. Wilcoxon signed-rank test.

*p < 0.05; ***p < 0.001; n.s., not significant. See also Figure S8.

delayed activation (dAct) groups (Figures 7D–7H and S9A-S9C). Most inhibition occurred within a short delay (inhibition trough: 8.2 ± 0.8 ms), consistent with monosynaptic inhibition by VIP neurons; and excitation occurred with a longer delay (excitation peak: 74.3 ± 4.4 ms) and broader temporal spread (Figure S9B), consistent with disynaptic or polysynaptic events.

(B) Typical field of view (FOV) under a 920-nm green channel to record Ca^{2+} activity (left and middle) and 1,030-nm red channel to locate JAWs-expressing neurons (right). White arrows indicate the neurons expressing both GCaMP6f and JAWs-tdTomato. Scale bars, 20 μm.

(C) Cell fields under the 920-nm (left, middle) and 1,030-nm (right) channel in PV::tdTomato (left) or PV::JAWs (middle and right) mice during 635-nm light stimulation, which activates the inhibitory opsin JAWs in PV::JAWs mice. Cells are color coded to reveal increase (red) or decrease (blue) in Ca^{2+} transient rates. Change index is defined as (light on − light off)/(light on + light off), such that a value > 0 means activation, and < 0 means inhibition during light on.

(D and I) Representative raw Ca^{2+} traces of neurons marked in (C) or (H). Note that neurons 1 and 2 are PV+ (D) or VIP+ neurons (I), since they express both GCaMP6f and JAWs. They are inhibited during light on. Neurons 3–5 are putative non-PV (D) or non-VIP (I) since they only express GCaMP6f.

(E and J) Heatmaps showing average responses of PV+ and non-PV (E) or VIP+ and non-VIP (J) neurons that show a significant change in Ca^{2+} signals during JAWs-mediated photoinhibition.

(F and K) Fraction of PV+ and non-PV (F) or VIP+ and non-VIP (K) neurons that show a significant increase, decrease, or no change upon JAWs-mediated photoinhibition. Wilcoxon matched-pairs signed-rank test, p < 0.05.

(G and L) Fold change of Ca^{2+} event transients of non-PV (G) or non-VIP (L) neurons during photoinhibition of PV (G) or VIP (L) neurons. Two-way repeated-measure ANOVA, **p < 0.01. N represents the number of mice; n represents the number of neurons.

(H) Cell fields under 920-nm (left, middle) and 1,030-nm (right) channel in VIP::tdTomato (left) or VIP::JAWs (middle and right) mice during 635-nm light stimulation, which activates the inhibitory opsin JAWs in VIP::JAWs mice. Cells are color coded to reveal increase (red) or decrease (blue) in Ca^{2+} transient rates.

Error bars indicate ± SEM. **p < 0.01. See also Figures S6 and S7.

Please cite this article in press as: Zhang et al., Dynamics of a disinhibitory prefrontal microcircuit in controlling social competition, Neuron (2021), https://doi.org/10.1016/j.neuron.2021.10.034

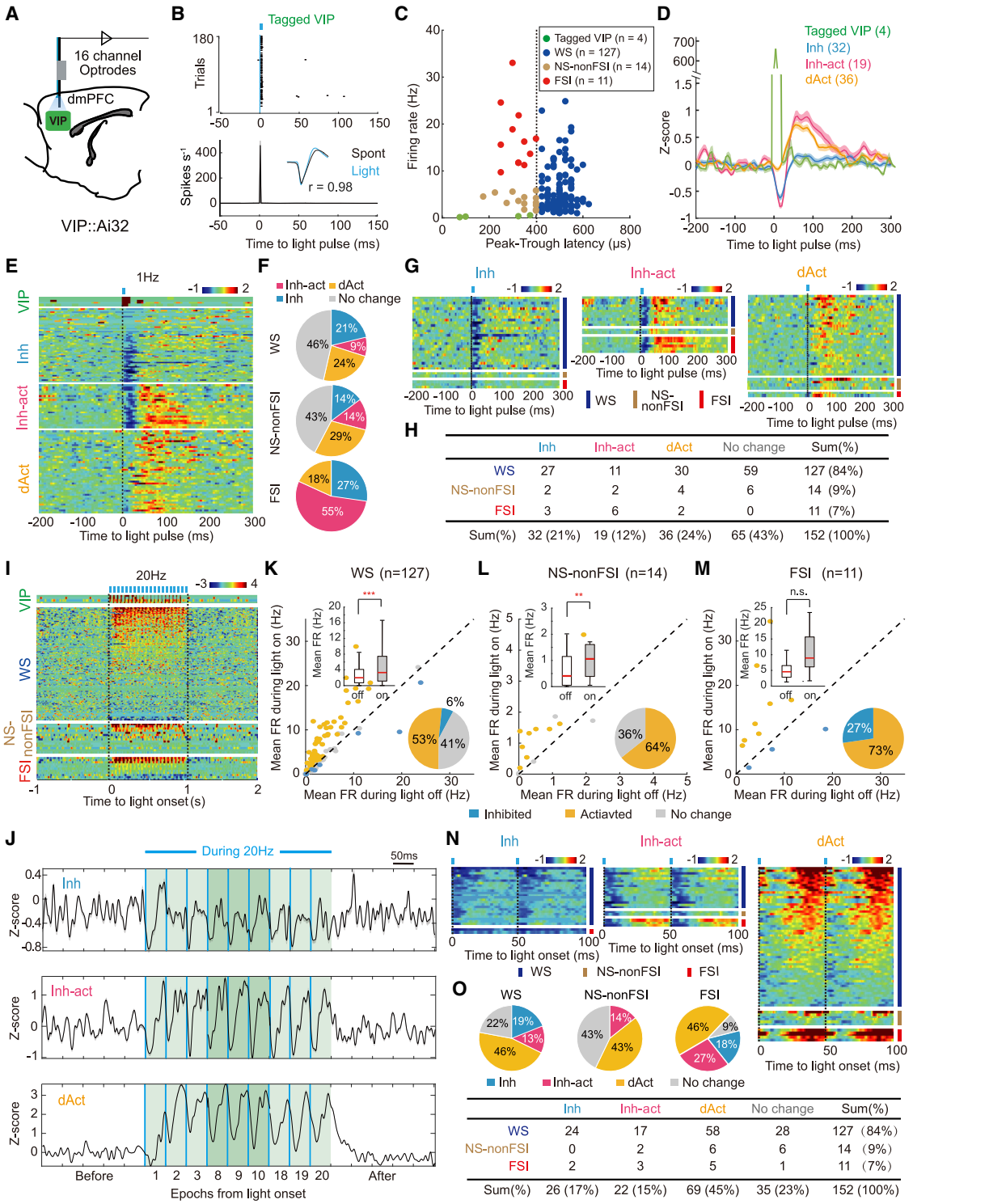

Figure 7. Effects of activating VIP neurons on dmPFC neural network activity

(A) Schematic illustration of *in vivo* optrode recording in the dmPFC of VIP-Cre::Ai32 mice.

(B) Raster plot (top) and PSTH (bottom) of a representative tagged VIP neuron. The inset shows that light-evoked spike waveforms (blue) were similar to spontaneous ones (black). Pearson's correlation, r = 0.98.

(C) Baseline firing rate versus peak-to-trough latency of tagged VIP (green), WS (blue), NS non-FSI (brown), and FSI (red) neurons.

(legend continued on next page)

Please cite this article in press as: Zhang et al., Dynamics of a disinhibitory prefrontal microcircuit in controlling social competition, Neuron (2021), https://doi.org/10.1016/j.neuron.2021.10.034

We then applied the 20-Hz light stimulation protocol, which successfully increased the tube test rank, in *in vivo* recording (Figures 1M-1O, 7I, and 7J). During the whole 1-s period of VIP neuron photostimulation, more pPYR neurons were excited than those being inhibited (pPYRs: 53% excited, 6% inhibited; Figures 7K and S9D). The average activity of WS pPYR neurons was increased by 60% during photostimulation of VIP neurons (Figures 7I and 7K). A similar trend of change occurred in pIN neurons, including NS non-FSI (64% excited, 0% inhibited, Figure 7L) and FSI (73% excited, 27% inhibited; Figure 7M) types. After each light pulse, of all the excited neurons, a small portion showed an immediate transient inhibition followed by excitation (Inh-act) but a majority (76%) of them showed delayed activation (dAct) (Figures 7N and 7O). Again, the inhibition occurred with a monosynaptic inhibition trough (3.7 ± 0.3 ms), and activation followed with a polysynaptic excitation peak (36.5 ± 0.8 ms) (Figures S9E and S9F). Despite the overall similarity in triggering neuronal responses, compared with the 1-Hz protocol, the 20-Hz stimulation protocol yielded a greatly reduced number of nonresponsive neurons (23% versus 43% of total neurons; Figures 7H and 7O) and a much larger fraction of dAct neurons (45% versus 24% of total neurons; Figures 7H and 7O), suggesting that at the behaviorally relevant stimulation frequency, VIP activation may activate a larger fraction of the network. It is also worth noting that VIP activation inhibited a significant fraction of FSI (pPV) neurons (Figures 7F and 7M), which could potentially mediate disinhibition onto other neuron types, including the PYR neurons.

Since the inhibition of pPV by VIP neurons is transient in nature (Figures 7G and 7H), we next tested the impact of transient inactivation of PV neurons on the PYR network. For that, we performed *in vivo* optrode recording in PV::eNpHR3.0 mice (Figure S10A), and we applied 1-Hz, 10-ms yellow light in the dmPFC to transiently inhibit PV interneurons. This led to the transient activation of a significant fraction (52%, n = 171) of pPYR neurons (Figure S10B and S10C).

The dynamic response of pPV and pPYR neurons during social competition

In the Ca^{2+} photometry experiment, we were not able to observe the transient inhibition of PV or PYR neurons during push initiation (Figure 4J). This may be due to the very transient (lasting 10–20 ms) nature of the inhibition and the relatively low temporal resolution of Ca^{2+} signal recording. To further dissect the dynamic relationship of PV and PYR neuron in social competition in behaving mice, we used a movable optrode to perform single-unit recording in PV-Cre::Ai32 mice during tube tests (Figure S11A). Putative PV and PYR neurons from layer V/VI were targeted and identified based on their responses to blue light pulses and waveform classification (Figures S11B and S11C; see STAR Methods). Among the 361 isolated units, there were 267 WS units, 50 non-FSI NS units, 21 FSIs, and 23 opto-tagged PV neurons. Both opto-tagged PV neurons and FSIs were combined as pPV neurons (n = 44, 12.2% of all recorded units) and their activities during the tube test were aligned to manual annotation of push epochs. Among these 44 pPV neurons, 17 (39%) increased firing and 9 (20%) decreased firing at the push onset (defined by firing change at -0.5 to 0.5 s around push onset; see STAR Methods, Figures S11D–S11F). Similar heterogeneity also exists in pPYR neurons (Figures S11G–S11I). In order to compare the precise onset time of neural activity change, we aligned the time point of significant change for pPV and pPYR neurons and found that the inhibition of push-inhibited pPV neurons precedes the excitation of the push-excited pPYR neurons ($p = 0.03$, Kolmogorov-Smirnov two-sample test; Figures S11J–S11L). We also did the same analysis for the push-excited pPV neurons, revealing that the distribution of the excitation onset time of push-excited pPV neurons aligns with that of push-excited pPYR neurons ($p = 0.63$, Kolmogorov-Smirnov two-sample test; Figures S11J, S11K, and S11M), and it lags behind that of push-inhibited pPV neurons ($p = 0.02$, Kolmogorov-Smirnov two-sample test; Figures S11J, S11K, and S11N). Therefore,

(D) Average PSTH of the tagged VIP (green), Inh (inhibition, blue), Inh-act (inhibition-activation, magenta), and dAct (delayed activation, orange) neuron groups. Shaded areas define ± SEM. Three well-separated groups are classified on the basis of light responsiveness in the 1-Hz, 1-ms protocol. Activation and inhibition are defined based on comparison with the baseline activity. See STAR Methods for definition of the three groups of neurons.

(E) PSTHs of all recorded neurons, including tagged VIP, Inh, Inh-act, and dAct neurons in the 1-Hz protocol. Vertical dashed lines delineate the time when the LED was turned on.

(F) Pie graphs showing the percentage of the Inh (blue), Inh-act (magenta), dAct (orange), and no change (gray) neurons, classified on the basis of light responsiveness within the 1-Hz protocol in WS (top), NS non-FSI (middle), and FSI (bottom) neurons, respectively.

(G) PSTHs of Inh (left), Inh-act (middle), and dAct (right) types within the WS (top), NS non-FSI (middle), and FSI (bottom) neurons.

(H) Summary of the number of neuron types under the 1-Hz protocol.

(I) PSTHs of all recorded neurons, including tagged VIP, nontagged WS, NS non-FSI, and FSI neurons in the 1-s, 20-Hz protocol. Neurons are ranked by a descending order of firing rate during the 1-s light-on period. Vertical dashed lines delineate the time when the 1-s stimulation protocol started and ended.

(J) Temporal expansion of the PSTH of the Inh (top), Inh-act (middle), and dAct (bottom) neurons during the 20-Hz stimulation. The average neuronal response of each neural group during the beginning (epochs 1–3), middle (epochs 8–10), and end (epochs 18–20) is displayed to show that responses were largely invariable from the beginning to end of light stimulation. Vertical blue lines delineate the time when the LED was turned on.

(K–M) Scatterplots of the mean firing rates of WS (K), NS non-FSI (L), and FSI (M) neurons during the 1-s light-on epoch, plotted against firing rates during the 1-s light-off epoch. Colored circles indicate neurons that showed a significant light-induced firing rate increase (orange) or decrease (blue). Inset pie graphs show the percentage of neurons that were significantly inhibited (blue), activated (orange), or unchanged (gray) during the light stimulation. Inhibition and activation are defined in comparison with the baseline firing rate during the 1-s light-off epoch. Inset boxplots show the overall firing rate during the 1-s light-off and 1-s light-on epoch. Data in all figures are median ± 1.5× interquartile range. Wilcoxon signed-rank test.

(N) PSTHs of Inh (left), Inh-act (middle), and dAct (right) types within the WS (top), NS non-FSI (middle), and FSI (bottom) neurons.

(O) Pie graph (top) and table (bottom) summary of the number of neuron types in each category under the 20-Hz, 5-ms protocol.

**$p < 0.01$; ***$p < 0.001$; n.s., not significant. See also Figures S8 and S9.

Please cite this article in press as: Zhang et al., Dynamics of a disinhibitory prefrontal microcircuit in controlling social competition, Neuron (2021), https://doi.org/10.1016/j.neuron.2021.10.034

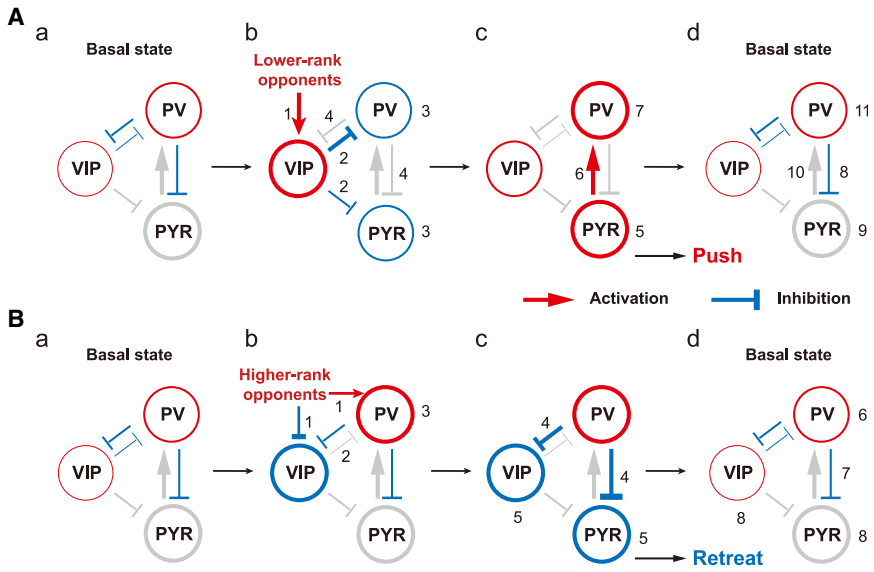

Figure 8. A model depicting the dynamic change of the dmPFC microcircuit in social competition

(A–Bd) Working model of the dynamics of the dmPFC microcircuit during pushes (A) and retreats (B). Under the basal state, there is balanced excitation and inhibition among VIP, PV, and PYR neurons. PV neurons have relatively high basal activity and exert a mild tonic inhibition onto other neurons (Aa). During pushes, VIP neurons are activated first, leading to transient inhibition of both PV and PYR neurons (Ab). Inhibition of PV leads to disinhibition of VIP and PYR, whose activity will lead to push behaviors. The recurrent activity of PYR also excites PV (Ac). The feedback inhibition from PV eventually tips the network balance toward the basal state (Ad). During retreats, either due to inhibition of VIP neurons or input from other upstream signals, PV neurons are activated (Bb). Their activity inhibits VIP and PYR neurons (Bc). Ending of the input signal brings network activity back to the basal state (Bd). Numbers on arrows indicate the sequence of events. Red indicates activation, and blue indicates inhibition. The thickness of lines and circles indicates the level of activation or inhibition.

there is clear heterogeneity in the response and temporal dynamics of pPV and pPYR neurons during the push onset. Furthermore, a fraction of PV neurons has the potential to mediate the disinhibition of PYR neurons during push onset in social competition.

DISCUSSION

Using cell-type-specific Ca^{2+} imaging, electrophysiological, optogenetic, and chemogenetic tools, we studied the function of major dmPFC interneuron types in the regulation of dominance behaviors. In conspecific competitions modeled by the dominance tube test, we found that dmPFC VIP and PV neurons play opposing functions in regulating pushes and retreats. Calcium signal dynamics during tube tests suggested that during pushes, dmPFC VIP neurons are activated earlier and more transiently than PV or PYR neurons. During retreats, dmPFC-PV neurons are activated, whereas VIP or PYR neurons are inhibited. Dual-color miniature two-photon microscopy combined with optogenetic manipulation confirmed that VIP and PV neurons oppositely regulate dmPFC neural network activity in awake mice. Furthermore, optrode recordings revealed response dynamics of different neuron types under a physiological pattern of VIP or PV activation. Based on this collection of data and knowledge from previous reports, we propose a working model to delineate the sequential action of the VIP, PV, and PYR neurons within the dmPFC microcircuits during social competition (Figure 8). Under the basal state, PV neurons have relatively high basal activity (Figure 6C) and exert a mild tonic inhibition onto other neurons (Figure 8Aa). During pushes, VIP neurons are activated (Figures 4J and 8Ab), leading to transient inhibition of both PV and PYR neurons (Figures 7E and 8Ab). Inhibition of PV then leads to disinhibition of PYR (Figures 5E and 8Ac), whose activity can be sustained for a period of time through recurrent activation (Douglas et al., 1995). PYR activation also excites PV (Figure 8Ac), whose feedback inhibition eventually brings all neurons back to their basal state (Figure 8Ad) (Couey et al., 2013; Ozeki et al., 2009). During retreats, either due to inhibition of VIP neurons or input from other upstream signals, PV neurons are activated (Figures 4K and 8Bb). Their activity globally inhibits neurons in the dmPFC network (Figures 6 and 8Bc). The return to basal state can be achieved through autoinhibition of PV neurons (Figure 8Bd) (Bacci and Huguenard, 2006; Pfeffer et al., 2013). Through these dynamic interactions, the interneurons and pyramidal neurons in the dmPFC network orchestrate winning- and losing-related behaviors in social competition. Specifically, we highlight a disinhibitory microcircuit in this process from VIP to PYR neurons mediated by PV interneurons.

Role of VIP interneurons

VIP interneurons have been demonstrated to disinhibit PYR neurons in various neural circuits (e.g., visual cortex, auditory cortex, amygdala, mPFC) and in the context of a wide range of behavioral performances, ranging from fear learning (Krabbe et al., 2019; Letzkus et al., 2011), reinforcement learning (Pi et al., 2013), visual information processing (Fu et al., 2014; Zhang et al., 2014), motor performance (Garcia-Junco-Clemente et al., 2017), to avoidance (Lee et al., 2019), short-term memory (Kamigaki and Dan, 2017), and spatial reward learning (Turi et al., 2019). Adding to this general theme, our results demonstrate that VIP-mediated disinhibition of the dmPFC PYR neurons plays an instrumental role in regulating motivational behaviors during conspecific social competition. Our Ca^{2+} imaging recording reveals that VIP neurons are activated earlier and more transiently than PV and PYR neurons in the dmPFC during pushes. This temporal characteristic is consistent with the proposal that VIP interneurons may be involved in the initial stages of cortical

Please cite this article in press as: Zhang et al., Dynamics of a disinhibitory prefrontal microcircuit in controlling social competition, Neuron (2021), https://doi.org/10.1016/j.neuron.2021.10.034

information processing (Fu et al., 2014; Khan et al., 2018; Staiger et al., 1996; Zhang et al., 2014). VIP interneurons receive inputs from the sensory thalamus (Lee et al., 2013; Staiger et al., 1996; Wall et al., 2016), long-range cortical projections (Ährlund-Richter et al., 2019; Lee et al., 2013; Sun et al., 2019; Zhang et al., 2014), as well as the cholinergic basal forebrain (Ährlund-Richter et al., 2019; Alitto and Dan, 2013; Askew et al., 2019; Prönneke et al., 2020). Integrating these sensory, intercortical, and neuromodulatory inputs, VIP may initiate a cascade of signal propagation in the mPFC microcircuits, thus releasing principal cells from inhibition and enabling a top-down control of effortful behaviors during social competition.

Role of PV interneurons

Downstream of VIP, which cell type(s) may mediate its disinhibitory effects onto PYR neurons? While some previous work implicated SOM neurons in this disinhibitory process such as in the barrel cortex (Lee et al., 2013), in social competition and in dmPFC, our manipulation data suggest PV neurons instead to be a strong candidate (Figures 1 and 2). Furthermore, as revealed in our optrode recordings, the activation/inhibition dynamics of PV neurons also align with such a mediator role. When analyzing the electrophysiological characteristics of neurons that were immediately inhibited upon VIP-specific photostimulation, among the 51 (of 152 neurons recorded) inhibited and Inh-act neurons, there were 4 NS non-FS pINs and 9 FSI pPV neurons, which showed inhibition within a 10-ms, monosynaptic delay (Figures 7G and 7H). Furthermore, in behaving mice, we identified a subpopulation of push-inhibited pPV neurons whose firing decrease preceded a firing increase of the push-activated pPYR neurons (Figures S11J and S11K). Therefore, some pPV neurons are inhibited at the right time point to potentially mediate the disinhibition of PYR by VIP neurons.

Although the connectivity from VIP to PV neurons may be sparse, as shown by recordings in cortical brain slices (Ährlund-Richter et al., 2019; Lee et al., 2013; Pfeffer et al., 2013; Pi et al., 2013), there have been reports of PV neurons functionally mediating the disinhibitory effect of VIP neurons in various neural circuits. In the deep layer of the barrel cortex, PV neurons are strongly inhibited when upper-layer VIP neurons are stimulated, and this direct inhibition may overpower the indirect disinhibitory VIP-SST-PV pathway (Yu et al., 2019). In the basolateral amygdala, VIP disinhibits PYRs through inhibition of both SOM and PV neurons, with comparable connectivity (Krabbe et al., 2019). In the mPFC, VIP inhibits a significant fraction (25%) of PV neurons (Pi et al., 2013) and the firing rates of PV neurons reversely correlate with the amount of VIP input (Lagler et al., 2016). In the hippocampus, learning-induced network plasticity is mediated by increased VIP to PV transmission (Donato et al., 2013). Because VIP neurons mainly target on the somatic compartment of PV neurons, their regulation can be highly effective (Hioki et al., 2013, 2018). Furthermore, due to their extensive targeting and unique morphological and electrophysiological features, PV neurons can connect with a large number of cells, allowing an enormous level of feedforward and feedback inhibition (Hu et al., 2014; Packer and Yuste, 2011). Thus, inhibition of a limited number of PV neurons has the potential to have an extensive impact on network activity.

In our Ca^{2+} photometry experiment, PV neurons showed a general increase in activity during the later phase of push epochs (Figure 4I). This counterintuitive excitation is predicted in our working model: once PYR neurons are activated, their recurrent activity will quickly activate PV (Figure 8Ac). The quick rise in PV activity is consistent with the view that inhibitory activity closely tracks the activity of PYR neurons, which is necessary for maintaining the network's excitation-inhibition balance (Anderson et al., 2000; Okun and Lampl, 2008; Shu et al., 2003; Wehr and Zador, 2003; Xue et al., 2014).

Role of SOM interneurons

In the photometry recording experiment, SOM neurons in general showed a similar response in the tube tests as PV neurons but with a smaller amplitude of change (Figures S12 and 4G–4I). Although SOM neurons are capable of inhibiting PYR neurons in the mPFC (Kvitsiani et al., 2013; Scheggia et al., 2020; Yamamuro et al., 2020), unlike PV, either activation or inhibition of SOM neurons did not seem to have a significant impact on dominance tube competitions (Figures 1 and 2). One possible reason may be that SOM neurons have more heterogeneous functions, sending inhibitory outputs to both PYR and other interneuron types (Miao et al., 2016; Pfeffer et al., 2013; Xu et al., 2013) and thus exerting both inhibitory and disinhibitory functions onto PYR neurons (Cummings and Clem, 2020; Xu et al., 2019). However, despite the lack of behavioral effects when activating or inhibiting dmPFC SOM as a whole group, we do not rule out the possibility that subpopulations of SOM may be involved in the process. Although not depicted in our working model (Figure 8), it is quite likely that some SOM and other interneurons may also contribute to the microcircuit dynamics underlying social competition. In the future, studies using a Cre- and Flp-dependent intersectional approach (which allows simultaneous recording of one cell type while manipulating another type) will help to delineate a clearer picture of the dmPFC microcircuit dynamics in social competition.

STAR★METHODS

Detailed methods are provided in the online version of this paper and include the following:

- KEY RESOURCES TABLE
- RESOURCE AVAILABILITY
  - Lead contact
  - Materials availability
  - Data and code availability
- EXPERIMENTAL MODEL AND SUBJECT DETAILS
  - Animals
- METHOD DETAILS
  - Viral injection and fiber implantation
  - Behavioral assays
  - Immunohistochemistry
  - Fiber photometry recording
  - Acute *in vivo* optrode recording in head-fixed mice
  - Chronic *in vivo* optrode recording on PV-Cre::ChR2 mice
  - Spike sorting and unit classification with optogenetic tagging

SUPPLEMENTAL INFORMATION

Supplemental information can be found online at https://doi.org/10.1016/j.neuron.2021.10.034.

ACKNOWLEDGMENTS

We thank Qiye He, Min Chen, and Melissa Skibba for discussions and comments on the manuscript; Shiqi Wang, Fei Wang, Hexin Liang, Baixiu Zheng, and Jiarui Chang for assistance in experiments; Karl Deisseroth and Zilong Qiu for AAV-ChR2 constructs; Xiaohui Zhang, Xiaohong Xu, and Xiang Yu for Cre mice; the Nanjing Brain Observatory for FHIRM-TPM V2.0 observation and two-photon data processing services; and Xinkuan Xiang, Lin Liu, and Yi Li for advice on data analysis. This work was supported by grants from the National Natural Science Foundation of China (81527901 and 31830032), the Key-Area Research and Development Program of Guangdong Province (2018B030334001 and 2018B030331001), the nonprofit Central Research Institute Fund of the Chinese Academy of Medical Sciences (2017PT31038 and 2018PT31041), the National Key Research and Development Program of China (2016YFA0501000), the 111 Project (B13026), the Fountain-Valley Life Sciences Fund of University of Chinese Academy of Sciences Education Foundation and the CAMS Innovation Fund for Medical Sciences (2019-I2M-5-057), the Key R&D Program of Zhejiang Province (2020C03009), and the Starry Night Science Fund of Zhejiang University Shanghai Institute for Advanced Study (SN-ZJU-SIAS-002).

AUTHOR CONTRIBUTIONS

H.H., H.Z., and C.Z. designed the study and analyzed data. H.Z., T.Z., Q.X., and C.Z. performed optogenetic and chemogenetic manipulation and related behavioral analysis. C.Z., H.Z., and Q.X. performed fiber photometry recording experiments and *in vivo* optrode recording. Z.N. wrote most MATLAB scripts for fiberphotometry and *in vivo* optrode recording data analysis. C.Z. and R.W. performed two-photon imaging data acquisition and analysis supported by the Nanjing Brain Observatory under the supervision of J.Z. and H.C.; G.G., Z.G., H.M., H.L., and M.H. contributed reagents and discussions. H.H. wrote the manuscript with the help of C.Z., H.Z., and Z.N.

DECLARATION OF INTERESTS

H.H. is a member of the advisory board of *Neuron*.

Received: March 22, 2021
Revised: August 12, 2021
Accepted: October 22, 2021
Published: November 17, 2021

REFERENCES

Ährlund-Richter, S., Xuan, Y., van Lunteren, J.A., Kim, H., Ortiz, C., Pollak Dorocic, I., Meletis, K., and Carlén, M. (2019). A whole-brain atlas of monosynaptic input targeting four different cell types in the medial prefrontal cortex of the mouse. Nat. Neurosci. *22*, 657–668.

Alitto, H.J., and Dan, Y. (2013). Cell-type-specific modulation of neocortical activity by basal forebrain input. Front. Syst. Neurosci. *6*, 79.

Anderson, J.S., Carandini, M., and Ferster, D. (2000). Orientation tuning of input conductance, excitation, and inhibition in cat primary visual cortex. J. Neurophysiol. *84*, 909–926.

Armbruster, B.N., Li, X., Pausch, M.H., Herlitze, S., and Roth, B.L. (2007). Evolving the lock to fit the key to create a family of G protein-coupled receptors potently activated by an inert ligand. Proc. Natl. Acad. Sci. USA *104*, 5163–5168.

Askew, C.E., Lopez, A.J., Wood, M.A., and Metherate, R. (2019). Nicotine excites VIP interneurons to disinhibit pyramidal neurons in auditory cortex. Synapse *73*, e22116.

Bacci, A., and Huguenard, J.R. (2006). Enhancement of spike-timing precision by autaptic transmission in neocortical inhibitory interneurons. Neuron *49*, 119–130.

Bailey, M.R., Simpson, E.H., and Balsam, P.D. (2016). Neural substrates underlying effort, time, and risk-based decision making in motivated behavior. Neurobiol. Learn. Mem. *133*, 233–256.

Bicks, L.K., Yamamuro, K., Flanigan, M.E., Kim, J.M., Kato, D., Lucas, E.K., Koike, H., Peng, M.S., Brady, D.M., Chandrasekaran, S., et al. (2020). Prefrontal parvalbumin interneurons require juvenile social experience to establish adult social behavior. Nat. Commun. *11*, 1003.

Blair, R.J., and Cipolotti, L. (2000). Impaired social response reversal. A case of 'acquired sociopathy'. Brain *123*, 1122–1141.

Boyden, E.S., Zhang, F., Bamberg, E., Nagel, G., and Deisseroth, K. (2005). Millisecond-timescale, genetically targeted optical control of neural activity. Nat. Neurosci. *8*, 1263–1268.

Cao, W., Lin, S., Xia, Q.Q., Du, Y.L., Yang, Q., Zhang, M.Y., Lu, Y.Q., Xu, J., Duan, S.M., Xia, J., et al. (2018). Gamma Oscillation Dysfunction in mPFC Leads to Social Deficits in Neuroligin 3 R451C Knockin Mice. Neuron *97*, 1253–1260.e7.

Chen, G., Zhang, Y., Li, X., Zhao, X., Ye, Q., Lin, Y., Tao, H.W., Rasch, M.J., and Zhang, X. (2017). Distinct Inhibitory Circuits Orchestrate Cortical beta and gamma Band Oscillations. Neuron *96*, 1403–1418.e6.

Chen, T.-W., Wardill, T.J., Sun, Y., Pulver, S.R., Renninger, S.L., Baohan, A., Schreiter, E.R., Kerr, R.A., Orger, M.B., Jayaraman, V., et al. (2013). Ultrasensitive fluorescent proteins for imaging neuronal activity. Nature *499*, 295–300.

Chuong, A.S., Miri, M.L., Busskamp, V., Matthews, G.A., Acker, L.C., Sørensen, A.T., Young, A., Klapoetke, N.C., Henninger, M.A., Kodandaramaiah, S.B., et al. (2014). Noninvasive optical inhibition with a red-shifted microbial rhodopsin. Nat. Neurosci. *17*, 1123–1129.

Couey, J.J., Witoelar, A., Zhang, S.J., Zheng, K., Ye, J., Dunn, B., Czajkowski, R., Moser, M.B., Moser, E.I., Roudi, Y., and Witter, M.P. (2013). Recurrent inhibitory circuitry as a mechanism for grid formation. Nat. Neurosci. *16*, 318–324.

Cummings, K.A., and Clem, R.L. (2020). Prefrontal somatostatin interneurons encode fear memory. Nat. Neurosci. *23*, 61–74.

Donato, F., Rompani, S.B., and Caroni, P. (2013). Parvalbumin-expressing basket-cell network plasticity induced by experience regulates adult learning. Nature *504*, 272–276.

Douglas, R.J., Koch, C., Mahowald, M., Martin, K.A., and Suarez, H.H. (1995). Recurrent excitation in neocortical circuits. Science *269*, 981–985.

Fan, Z., Zhu, H., Zhou, T., Wang, S., Wu, Y., and Hu, H. (2019). Using the tube test to measure social hierarchy in mice. Nat. Protoc. *14*, 819–831.

Fernald, R.D. (2014). Cognitive Skills Needed for Social Hierarchies. Cold Spring Harb. Symp. Quant. Biol. *79*, 229–236.

Flusberg, B.A., Cocker, E.D., Piyawattanametha, W., Jung, J.C., Cheung, E.L., and Schnitzer, M.J. (2005). Fiber-optic fluorescence imaging. Nat. Methods *2*, 941–950.

Franklin, T.B., Silva, B.A., Perova, Z., Marrone, L., Masferrer, M.E., Zhan, Y., Kaplan, A., Greetham, L., Verrechia, V., Halman, A., et al. (2017). Prefrontal cortical control of a brainstem social behavior circuit. Nat. Neurosci. *20*, 260–270.

Friard, O., and Gamba, M. (2016). BORIS: a free, versatile open-source event-logging software for video/audio coding and live observations. Methods Ecol. Evol. *7*, 1325–1330.

Friedman, A., Homma, D., Gibb, L.G., Amemori, K., Rubin, S.J., Hood, A.S., Riad, M.H., and Graybiel, A.M. (2015). A Corticostriatal Path Targeting Striosomes Controls Decision-Making under Conflict. Cell *161*, 1320–1333.

Fu, Y., Tucciarone, J.M., Espinosa, J.S., Sheng, N., Darcy, D.P., Nicoll, R.A., Huang, Z.J., and Stryker, M.P. (2014). A cortical circuit for gain control by behavioral state. Cell *156*, 1139–1152.

Fujii, N., Hihara, S., Nagasaka, Y., and Iriki, A. (2009). Social state representation in prefrontal cortex. Soc. Neurosci. *4*, 73–84.

Garcia-Junco-Clemente, P., Ikrar, T., Tring, E., Xu, X., Ringach, D.L., and Trachtenberg, J.T. (2017). An inhibitory pull-push circuit in frontal cortex. Nat. Neurosci. *20*, 389–392.

Gunaydin, L.A., Grosenick, L., Finkelstein, J.C., Kauvar, I.V., Fenno, L.E., Adhikari, A., Lammel, S., Mirzabekov, J.J., Airan, R.D., Zalocusky, K.A., et al. (2014). Natural neural projection dynamics underlying social behavior. Cell *157*, 1535–1551.

Hattori, R., Kuchibhotla, K.V., Froemke, R.C., and Komiyama, T. (2017). Functions and dysfunctions of neocortical inhibitory neuron subtypes. Nat. Neurosci. *20*, 1199–1208.

Hillman, K.L., and Bilkey, D.K. (2012). Neural encoding of competitive effort in the anterior cingulate cortex. Nat. Neurosci. *15*, 1290–1297.

Hioki, H., Okamoto, S., Konno, M., Kameda, H., Sohn, J., Kuramoto, E., Fujiyama, F., and Kaneko, T. (2013). Cell type-specific inhibitory inputs to dendritic and somatic compartments of parvalbumin-expressing neocortical interneuron. J. Neurosci. *33*, 544–555.

Hioki, H., Sohn, J., Nakamura, H., Okamoto, S., Hwang, J., Ishida, Y., Takahashi, M., and Kameda, H. (2018). Preferential inputs from cholecystokinin-positive neurons to the somatic compartment of parvalbumin-expressing neurons in the mouse primary somatosensory cortex. Brain Res. *1695*, 18–30.

Hippenmeyer, S., Vrieseling, E., Sigrist, M., Portmann, T., Laengle, C., Ladle, D.R., and Arber, S. (2005). A developmental switch in the response of DRG neurons to ETS transcription factor signaling. PLoS Biol. *3*, e159.

Holroyd, C.B., and McClure, S.M. (2015). Hierarchical control over effortful behavior by rodent medial frontal cortex: A computational model. Psychol. Rev. *122*, 54–83.

Hosokawa, T., and Watanabe, M. (2012). Prefrontal neurons represent winning and losing during competitive video shooting games between monkeys. J. Neurosci. *32*, 7662–7671.

Hu, H., Gan, J., and Jonas, P. (2014). Interneurons. Fast-spiking, parvalbumin^{+} GABAergic interneurons: from cellular design to microcircuit function. Science *345*, 1255263.

Hua, R., Wang, X., Chen, X., Wang, X., Huang, P., Li, P., Mei, W., and Li, H. (2018). Calretinin Neurons in the Midline Thalamus Modulate Starvation-Induced Arousal. Curr. Biol. *28*, 3948–3959.e4.

Huang, Z.J. (2014). Toward a genetic dissection of cortical circuits in the mouse. Neuron *83*, 1284–1302.

Kamigaki, T., and Dan, Y. (2017). Delay activity of specific prefrontal interneuron subtypes modulates memory-guided behavior. Nat. Neurosci. *20*, 854–863.

Kepecs, A., and Fishell, G. (2014). Interneuron cell types are fit to function. Nature *505*, 318–326.

Kerlin, A.M., Andermann, M.L., Berezovskii, V.K., and Reid, R.C. (2010). Broadly tuned response properties of diverse inhibitory neuron subtypes in mouse visual cortex. Neuron *67*, 858–871.

Khan, A.G., Poort, J., Chadwick, A., Blot, A., Sahani, M., Mrsic-Flogel, T.D., and Hofer, S.B. (2018). Distinct learning-induced changes in stimulus selectivity and interactions of GABAergic interneuron classes in visual cortex. Nat. Neurosci. *21*, 851–859.

Kim, H., Ährlund-Richter, S., Wang, X., Deisseroth, K., and Carlén, M. (2016). Prefrontal Parvalbumin Neurons in Control of Attention. Cell *164*, 208–218.

Kingsbury, L., Huang, S., Raam, T., Ye, L.S., Wei, D., Hu, R.K., Ye, L., and Hong, W. (2020). Cortical Representations of Conspecific Sex Shape Social Behavior. Neuron *107*, 941–953.e7.

Krabbe, S., Paradiso, E., d'Aquin, S., Bitterman, Y., Courtin, J., Xu, C., Yonehara, K., Markovic, M., Müller, C., Eichlisberger, T., et al. (2019). Adaptive disinhibitory gating by VIP interneurons permits associative learning. Nat. Neurosci. *22*, 1834–1843.

Kvitsiani, D., Ranade, S., Hangya, B., Taniguchi, H., Huang, J.Z., and Kepecs, A. (2013). Distinct behavioural and network correlates of two interneuron types in prefrontal cortex. Nature *498*, 363–366.

Lagler, M., Ozdemir, A.T., Lagoun, S., Malagon-Vina, H., Borhegyi, Z., Hauer, R., Jelem, A., and Klausberger, T. (2016). Divisions of Identified Parvalbumin-Expressing Basket Cells during Working Memory-Guided Decision Making. Neuron *91*, 1390–1401.

Lee, A.T., Cunniff, M.M., See, J.Z., Wilke, S.A., Luongo, F.J., Ellwood, I.T., Ponnavolu, S., and Sohal, V.S. (2019). VIP Interneurons Contribute to Avoidance Behavior by Regulating Information Flow across Hippocampal-Prefrontal Networks. Neuron *102*, 1223–1234.e4.

Lee, S., Kruglikov, I., Huang, Z.J., Fishell, G., and Rudy, B. (2013). A disinhibitory circuit mediates motor integration in the somatosensory cortex. Nat. Neurosci. *16*, 1662–1670.

Letzkus, J.J., Wolff, S.B., Meyer, E.M., Tovote, P., Courtin, J., Herry, C., and Lüthi, A. (2011). A disinhibitory microcircuit for associative fear learning in the auditory cortex. Nature *480*, 331–335.

Li, Y., Zhong, W., Wang, D., Feng, Q., Liu, Z., Zhou, J., Jia, C., Hu, F., Zeng, J., Guo, Q., et al. (2016). Serotonin neurons in the dorsal raphe nucleus encode reward signals. Nat. Commun. *7*, 10503.

Lindzey, G., Winston, H., and Manosevitz, M. (1961). Social dominance in inbred mouse strains. Nature *191*, 474–476.

Madisen, L., Mao, T., Koch, H., Zhuo, J.M., Berenyi, A., Fujisawa, S., Hsu, Y.W., Garcia, A.J., 3rd, Gu, X., Zanella, S., et al. (2012). A toolbox of Cre-dependent optogenetic transgenic mice for light-induced activation and silencing. Nat. Neurosci. *15*, 793–802.

Mah, L., Arnold, M.C., and Grafman, J. (2004). Impairment of social perception associated with lesions of the prefrontal cortex. Am. J. Psychiatry *161*, 1247–1255.

Miao, Q., Yao, L., Rasch, M.J., Ye, Q., Li, X., and Zhang, X. (2016). Selective Maturation of Temporal Dynamics of Intracortical Excitatory Transmission at the Critical Period Onset. Cell Rep. *16*, 1677–1689.

Mooney, S.J., Peragine, D.E., Hathaway, G.A., and Holmes, M.M. (2014). A game of thrones: neural plasticity in mammalian social hierarchies. Soc. Neurosci. *9*, 108–117.

Nelson, A.C., Kapoor, V., Vaughn, E., Gnanasegaram, J.A., Rubinstein, N.D., Murthy, V.N., and Dulac, C. (2019). Molecular and circuit architecture of social hierarchy. bioRxiv, 838664. https://doi.org/10.1101/838664.

Okun, M., and Lampl, I. (2008). Instantaneous correlation of excitation and inhibition during ongoing and sensory-evoked activities. Nat. Neurosci. *11*, 535–537.

Ozeki, H., Finn, I.M., Schaffer, E.S., Miller, K.D., and Ferster, D. (2009). Inhibitory stabilization of the cortical network underlies visual surround suppression. Neuron *62*, 578–592.

Packer, A.M., and Yuste, R. (2011). Dense, unspecific connectivity of neocortical parvalbumin-positive interneurons: a canonical microcircuit for inhibition? J. Neurosci. *31*, 13260–13271.

Pfeffer, C.K., Xue, M., He, M., Huang, Z.J., and Scanziani, M. (2013). Inhibition of inhibition in visual cortex: the logic of connections between molecularly distinct interneurons. Nat. Neurosci. *16*, 1068–1076.

Pi, H.J., Hangya, B., Kvitsiani, D., Sanders, J.I., Huang, Z.J., and Kepecs, A. (2013). Cortical interneurons that specialize in disinhibitory control. Nature *503*, 521–524.

Pinto, L., and Dan, Y. (2015). Cell-Type-Specific Activity in Prefrontal Cortex during Goal-Directed Behavior. Neuron *87*, 437–450.

Pnevmatikakis, E.A., and Giovannucci, A. (2017). NoRMCorre: An online algorithm for piecewise rigid motion correction of calcium imaging data. J. Neurosci. Methods *291*, 83–94.

Porter, B.S., Hillman, K.L., and Bilkey, D.K. (2019). Anterior cingulate cortex encoding of effortful behavior. J. Neurophysiol. *121*, 701–714.

Prönneke, A., Witte, M., Möck, M., and Staiger, J.F. (2020). Neuromodulation Leads to a Burst-Tonic Switch in a Subset of VIP Neurons in Mouse Primary Somatosensory (Barrel) Cortex. Cereb. Cortex *30*, 488–504.

Rudebeck, P.H., Buckley, M.J., Walton, M.E., and Rushworth, M.F. (2006). A role for the macaque anterior cingulate gyrus in social valuation. Science *313*, 1310–1312.

Rudebeck, P.H., Walton, M.E., Millette, B.H., Shirley, E., Rushworth, M.F., and Bannerman, D.M. (2007). Distinct contributions of frontal areas to emotion and social behaviour in the rat. Eur. J. Neurosci. *26*, 2315–2326.

Rudy, B., Fishell, G., Lee, S., and Hjerling-Leffler, J. (2011). Three groups of interneurons account for nearly 100% of neocortical GABAergic neurons. Dev. Neurobiol. *71*, 45–61.

Rushworth, M.F., Mars, R.B., and Sallet, J. (2013). Are there specialized circuits for social cognition and are they unique to humans? Curr. Opin. Neurobiol. *23*, 436–442.

Sandi, C., and Haller, J. (2015). Stress and the social brain: behavioural effects and neurobiological mechanisms. Nat. Rev. Neurosci. *16*, 290–304.

Sapolsky, R.M. (2005). The influence of social hierarchy on primate health. Science *308*, 648–652.

Scheggia, D., Managò, F., Maltese, F., Bruni, S., Nigro, M., Dautan, D., Latuske, P., Contarini, G., Gomez-Gonzalo, M., Requie, L.M., et al. (2020). Somatostatin interneurons in the prefrontal cortex control affective state discrimination in mice. Nat. Neurosci. *23*, 47–60.

Shu, Y., Hasenstaub, A., and McCormick, D.A. (2003). Turning on and off recurrent balanced cortical activity. Nature *423*, 288–293.

So, N., Franks, B., Lim, S., and Curley, J.P. (2015). A Social Network Approach Reveals Associations between Mouse Social Dominance and Brain Gene Expression. PLoS ONE *10*, e0134509.

Soltanian-Zadeh, S., Sahingur, K., Blau, S., Gong, Y., and Farsiu, S. (2019). Fast and robust active neuron segmentation in two-photon calcium imaging using spatiotemporal deep learning. Proc. Natl. Acad. Sci. USA *116*, 8554–8563.

Staiger, J.F., Zilles, K., and Freund, T.F. (1996). Innervation of VIP-immunoreactive neurons by the ventroposteromedial thalamic nucleus in the barrel cortex of the rat. J. Comp. Neurol. *367*, 194–204.

Stark, E., Eichler, R., Roux, L., Fujisawa, S., Rotstein, H.G., and Buzsáki, G. (2013). Inhibition-induced theta resonance in cortical circuits. Neuron *80*, 1263–1276.

Sun, Q., Li, X., Ren, M., Zhao, M., Zhong, Q., Ren, Y., Luo, P., Ni, H., Zhang, X., Zhang, C., et al. (2019). A whole-brain map of long-range inputs to GABAergic interneurons in the mouse medial prefrontal cortex. Nat. Neurosci. *22*, 1357–1370.

Taniguchi, H., He, M., Wu, P., Kim, S., Paik, R., Sugino, K., Kvitsiani, D., Fu, Y., Lu, J., Lin, Y., et al. (2011). A resource of Cre driver lines for genetic targeting of GABAergic neurons in cerebral cortex. Neuron *71*, 995–1013.

Tseng, W.T., Yen, C.T., and Tsai, M.L. (2011). A bundled microwire array for long-term chronic single-unit recording in deep brain regions of behaving rats. J. Neurosci. Methods *201*, 368–376.

Turi, G.F., Li, W.K., Chavlis, S., Pandi, I., O'Hare, J., Priestley, J.B., Grosmark, A.D., Liao, Z., Ladow, M., Zhang, J.F., et al. (2019). Vasoactive Intestinal Polypeptide-Expressing Interneurons in the Hippocampus Support Goal-Oriented Spatial Learning. Neuron *101*, 1150–1165.e8.

Varga, C., Golshani, P., and Soltesz, I. (2012). Frequency-invariant temporal ordering of interneuronal discharges during hippocampal oscillations in awake mice. Proc. Natl. Acad. Sci. USA *109*, E2726–E2734.

Wall, N.R., De La Parra, M., Sorokin, J.M., Taniguchi, H., Huang, Z.J., and Callaway, E.M. (2016). Brain-Wide Maps of Synaptic Input to Cortical Interneurons. J. Neurosci. *36*, 4000–4009.

Walton, M.E., Bannerman, D.M., and Rushworth, M.F. (2002). The role of rat medial frontal cortex in effort-based decision making. J. Neurosci. *22*, 10996–11003.

Wang, F., Kessels, H.W., and Hu, H. (2014). The mouse that roared: neural mechanisms of social hierarchy. Trends Neurosci. *37*, 674–682.

Wang, F., Zhu, J., Zhu, H., Zhang, Q., Lin, Z., and Hu, H. (2011). Bidirectional control of social hierarchy by synaptic efficacy in medial prefrontal cortex. Science *334*, 693–697.

Warden, M.R., Selimbeyoglu, A., Mirzabekov, J.J., Lo, M., Thompson, K.R., Kim, S.Y., Adhikari, A., Tye, K.M., Frank, L.M., and Deisseroth, K. (2012). A prefrontal cortex-brainstem neuronal projection that controls response to behavioural challenge. Nature *492*, 428–432.

Wehr, M., and Zador, A.M. (2003). Balanced inhibition underlies tuning and sharpens spike timing in auditory cortex. Nature *426*, 442–446.

Wilson, E.O. (2000). Sociobiology: the new synthesis (Cambridge: Belknap Press of Harvard University Press).

Xu, H., Jeong, H.Y., Tremblay, R., and Rudy, B. (2013). Neocortical somatostatin-expressing GABAergic interneurons disinhibit the thalamorecipient layer 4. Neuron *77*, 155–167.

Xu, H., Liu, L., Tian, Y., Wang, J., Li, J., Zheng, J., Zhao, H., He, M., Xu, T.L., Duan, S., and Xu, H. (2019). A Disinhibitory Microcircuit Mediates Conditioned Social Fear in the Prefrontal Cortex. Neuron *102*, 668–682.e5.

Xue, M., Atallah, B.V., and Scanziani, M. (2014). Equalizing excitation-inhibition ratios across visual cortical neurons. Nature *511*, 596–600.

Yamamuro, K., Bicks, L.K., Leventhal, M.B., Kato, D., Im, S., Flanigan, M.E., Garkun, Y., Norman, K.J., Caro, K., Sadahiro, M., et al. (2020). A prefrontal-paraventricular thalamus circuit requires juvenile social experience to regulate adult sociability in mice. Nat. Neurosci. *23*, 1240–1252.

Yizhar, O., Fenno, L.E., Prigge, M., Schneider, F., Davidson, T.J., O'Shea, D.J., Sohal, V.S., Goshen, I., Finkelstein, J., Paz, J.T., et al. (2011). Neocortical excitation/inhibition balance in information processing and social dysfunction. Nature *477*, 171–178.

Yu, J., Hu, H., Agmon, A., and Svoboda, K. (2019). Recruitment of GABAergic Interneurons in the Barrel Cortex during Active Tactile Behavior. Neuron *104*, 412–427.e4.

Zhang, S., Xu, M., Kamigaki, T., Hoang Do, J.P., Chang, W.C., Jenvay, S., Miyamichi, K., Luo, L., and Dan, Y. (2014). Selective attention. Long-range and local circuits for top-down modulation of visual cortex processing. Science *345*, 660–665.

Zhou, T., Sandi, C., and Hu, H. (2018). Advances in understanding neural mechanisms of social dominance. Curr. Opin. Neurobiol. *49*, 99–107.

Zhou, T., Zhu, H., Fan, Z., Wang, F., Chen, Y., Liang, H., Yang, Z., Zhang, L., Lin, L., Zhan, Y., et al. (2017). History of winning remodels thalamo-PFC circuit to reinforce social dominance. Science *357*, 162–168.

Zhu, H., and Hu, H. (2018). Brain's neural switch for social dominance in animals. Sci. China Life Sci. *61*, 113–114.

Zong, W., Wu, R., Chen, S., Wu, J., Wang, H., Zhao, Z., Chen, G., Tu, R., Wu, D., Hu, Y., et al. (2021). Miniature two-photon microscopy for enlarged field-of-view, multi-plane and long-term brain imaging. Nat. Methods *18*, 46–49.

Zong, W., Wu, R., Li, M., Hu, Y., Li, Y., Li, J., Rong, H., Wu, H., Xu, Y., Lu, Y., et al. (2017). Fast high-resolution miniature two-photon microscopy for brain imaging in freely behaving mice. Nat. Methods *14*, 713–719.

Please cite this article in press as: Zhang et al., Dynamics of a disinhibitory prefrontal microcircuit in controlling social competition, Neuron (2021), https://doi.org/10.1016/j.neuron.2021.10.034

STAR★METHODS

KEY RESOURCES TABLE

REAGENT or RESOURCE	SOURCE	IDENTIFIER
Antibodies		
Rabbit anti-CaMKII	Abcam	Cat# ab52476; RRID: AB_868641
Rabbit anti-parvalbumin	Swant	Cat# PV 27; RRID: AB_2631173
Rabbit anti-somatostatin	Peninsula Laboratories LLC	Cat# T-4103; RRID: AB_518614
Rabbit anti-vasoactive intestinal polypeptide	Immunostar	Cat# 20077; RRID: AB_572270
Chicken anti-GFP	Abcam	Cat# ab13970: RRID: AB_300798
Goat anti-rabbit Alexa Fluor 488	Thermo Fisher Scientific	Cat# A-11034; RRID:AB_2576217
Goat anti-chicken Alexa Fluor 488	Invitrogen	Cat# A-11039, RRID:AB_142924
Goat anti-rabbit Alexa Fluor 546	Invitrogen	Cat# A-11035, RRID:AB_143051
Bacterial and virus strains		
AAV2/9-CaMKIIα-ChR2(H134R)-mCherry	UPenn vector core	N/A
AAV2/9-EF1a-dflox-hChR2(H134R)-mCherry	Taitool Bioscience (Shanghai)	Cat# S0170-9-H20
AAV2/9-hEF1a-DIO-EYFP-WPRE-pA	Taitool Bioscience (Shanghai)	Cat# S0196-9-H50
AAV2/9-hSyn-double floxed hM4D(Gi)-mCherry	UMass Gao Lab Vector Core	N/A
AAV2/9-hSyn-GCaMP6s	Taitool Bioscience (Shanghai)	Cat# XT021
AAV2/9-Ubi-eGFP	UMass Gao Lab Vector Core	N/A
AAV2/9-CaMKIIα-GCaMP6s	Taitool Bioscience (Shanghai)	Cat# S0229-9-H20
AAV2/9-CAG-Flex-GCaMP6s	Taitool Bioscience (Shanghai)	Cat# S0354-9-H50
AAV2/9-Ef1a-DIO-eNpHR3.0-mCherry	ObioTechnology (Shanghai)	Cat# H4882
AAV2/9-hSyn-GCaMP6f	Taitool Bioscience (Shanghai)	Cat# SO224-9-H20
AAV2/9-EF1a-Flex-JAWs-tdTomato-ER2	Taitool Bioscience (Shanghai)	Cat# S0221-9-H20
Chemicals, peptides, and recombinant proteins		
Clozapine N-oxide (CNO)	Sigma	Cat# C0832
Experimental models: Organisms/strains		
C57BL/6J mice	SLAC Laboratory animal, Shanghai	N/A
Mouse: PV-Cre	Jackson Laboratory; Hippenmeyer et al. (2005)	Stock# 008069 (Gift from Xiaohui Zhang Lab)
Mouse: SST-Cre	Jackson Laboratory; Taniguchi et al. (2011)	Stock# 013044 (Gift from Xiang Yu Lab)
Mouse: VIP-Cre	Jackson Laboratory; Taniguchi et al. (2011)	Stock# 010908 (Gift from Xiaohong Xu Lab)
Mouse: Ai32	Jackson Laboratory; Madisen et al. (2012)	Stock# 024109
Software and algorithms		
OmniPlex neural recording data acquisition system	Plexon	https://plexon.com/products/omniplex-software
NeuroExplorer	Plexon	https://plexon.com/products/neuroexplorer
Offline sorter	Plexon	https://plexon.com/products/offline-sorter
MATLAB R2020a	MathWorks	https://www.mathworks.com/products/matlab.html
Custom analysis code	This paper	https://zenodo.org/record/5591050
Prism	GraphPad Software	https://www.graphpad.com/scientific-software/prism
ImageJ	National Institutes of Health	https://imagej.nih.gov/ij/index.html
BORIS	Friard and Gamba (2016)	http://www.boris.unito.it/
Other		
473nm and 589nm LED	Newdoon, Hangzhou	http://www.newdoon.com/cn/en/
Fiber photometry system	ThinkerTech, Nanjing	http://www.thinkerbiotech.com/

(*Continued on next page*)

Please cite this article in press as: Zhang et al., Dynamics of a disinhibitory prefrontal microcircuit in controlling social competition, Neuron (2021), https://doi.org/10.1016/j.neuron.2021.10.034

Continued

REAGENT or RESOURCE	SOURCE	IDENTIFIER
FHIRM-TPM V2.0	Chaoweijing Biological Technology (Beijing)	http://tv-scope.com/
Two- photon data processing	Nanjing Brain Observatory, NBO	http://www.raygenitm.com

RESOURCE AVAILABILITY

Lead contact

Further information and requests for resources and reagents may be directed to and will be fulfilled by the Lead Contact, Hailan Hu (huhailan@zju.edu.cn).

Materials availability

This study did not generate new unique reagents.

Data and code availability

- All data reported in this paper will be shared by the lead contact upon request.
- All original code has been deposited at Zenodo: https://zenodo.org/record/5591050 and is publicly available as of the date of publication. DOI are listed in the key resources table.
- Any additional information required to reanalyze the data reported in this paper is available from the lead contact upon request.

EXPERIMENTAL MODEL AND SUBJECT DETAILS

Animals

Adult (over 2 months old) male C57BL/6J (SLAC), VIP-Cre, PV-Cre, SOM-Cre mice (Hippenmeyer et al., 2005; Taniguchi et al., 2011) and offsprings of VIP-Cre, PV-Cre and SOM-Cre mice bred with Ai32 mice (Madisen et al., 2012) were used for experiments. Mice were housed in groups of 4 under standard housing conditions with food and water *ad libitum*. Animal use and care was under the guidelines of Zhejiang University.

METHOD DETAILS

Viral injection and fiber implantation

For virus injection, mice were anesthetized with ketamine (100 mg/kg, i.p.) and xylazine (8 mg/kg, i.p.) and mounted on a stereotaxic frame. For cell-type-specific optogenetic stimulation, AAV viruses were injected into the right dmPFC of wild-type mice (ML: 0.4 mm (from midline), AP: 2.43 mm (from bregma), DV: 1.2 mm (from dura)), and bilaterally into the dmPFC of PV-Cre and SOM-Cre (ML: ± 0.4 mm, AP: 2.43 mm, DV: 1.2 mm), and VIP-Cre (angle: 14°, ML: 0.71 mm, AP: 2.43 mm, DV: 1.67 mm) mice. Mono fiber-optic cannulae (AnniLab and Newdoon; for VIP::ChR2 and PYR::ChR2) or dual fiber-optic cannulae (Doric; for PV::ChR2 and SOM::ChR2 mice) were implanted on the same day or several days after viral injection. Coordinates for optic cannulae were 300 - 400 μm above viral injection coordinates, except that a coordinate further away from the midline (ML: ± 0.5 mm, AP: 2.43 mm, DV: 0.7∼0.8 mm) was used for the dual cannulae to target PV or SOM neurons, and a coordinate closer to midline (angle: 14°, ML: 0.71 mm, AP: 2.43 mm, DV: 1.3 mm) was used to target the superficial layer VIP- neurons. For chemogenetic inactivation, virus was injected into the bilateral dmPFC at the aforementioned coordinates. For fiber photometry experiments, virus was injected into the right hemisphere of the dmPFC at the aforementioned coordinates. Mono fiber-optic cannulae were implanted 300 μm above the virus injection site for fiber photometry. Mice were recovered from the surgeries for at least two weeks before any behavioral tests.

The following viruses were used: $AAV_{2/9}$-CaMKIIα-ChR2(H134R)-mCherry (titer: 3.41×10^{12} v.g./ml; no dilution; 0.2 μL for the right dmPFC; Addgene); $AAV_{2/9}$-EF1a-dflox-hChR2(H134R)-mCherry (titer: 1×10^{13} v.g./ml; dilution: 1:10; 0.2 μL per site in bilateral dmPFC of PV-Cre, VIP-Cre and SOM-Cre mice; UPenn vector core); $AAV_{2/9}$-hEF1a-DIO-EYFP-WPRE-pA (titer: 1.30×10^{13} v.g./ml; dilution: 1:10 for the right or bilateral dmPFC; Taitool Bioscience); $AAV_{2/9}$-hSyn-double floxed hM4D (Gi)-mCherry (titer:1×10^{13} v.g./ml; dilution: 1:8; 0.1 μL for bilateral dmPFC; UMass); $AAV_{2/9}$-hSyn-GCaMP6s (titer: 2.47×10^{13} v.g./ml; dilution: 1:10, 0.2 μL for the right dmPFC; Taitool Bioscience); $AAV_{2/9}$-Ubi-eGFP (titer: 2.50×10^{13} v.g./ml; dilution: 1:10 for the right dmPFC; UMass);$AAV_{2/9}$-CaMKIIα-GCaMP6s (titer: 1.23×10^{13} v.g./ml; dilution: 1:5; 0.2 μL for right dmPFC; Taitool Bioscience); $AAV_{2/9}$-CAG-Flex-GCaMP6s (titer: 3.75×10^{12} v.g./ml; 0.2 μL per site for the right dmPFC of PV-Cre mice and SOM-Cre mice and bilateral dmPFC of VIP-Cre mice; Taitool Bioscience); $AAV_{2/9}$-Ef1a-DIO-eNpHR3.0-mCherry (titer:2.41×10^{13} v.g./ml; dilution:1:10; 0.2 μl for right dmPFC; OBiO Technology).

Please cite this article in press as: Zhang et al., Dynamics of a disinhibitory prefrontal microcircuit in controlling social competition, Neuron (2021), https://doi.org/10.1016/j.neuron.2021.10.034

Behavioral assays

Tube test and video analysis

The tube test assay was applied as described before (Fan et al., 2019). Before the start of tube tests, mice were trained to go through the tube for 10 trials per day for 3 days. In test days, each pair of mice was released from the two ends of a tube (30 cm in length, 3 cm in diameter), meet at the middle, and the mouse that retreated first from the tube was designated as the "loser." Tube test trials were carried out between groups of 4 cagemates using a round robin design. The ranks were determined by total numbers of wining in each test day. Only mouse cages with stable ranks for over 3 successive days were used for further cell-type-specific optogenetic and chemogenetic manipulation.

By frame-to-frame video analysis, three forms of behaviors in total can be unambiguously identified from the meeting point to the end of each tube test trial: push (one mouse shoves its head under another mouse), resistance (hold on to the territory when being pushed, head often being pushed up), retreat (back out after being pushed or voluntarily withdraw, often characterized by bending down of head). These behavior epochs were manually annotated and marked by the BORIS software (Friard and Gamba, 2016).

Optogenetic activation of dmPFC neurons in tube test

A 12 mm slit was opened at the top of the tube to permit mice wearing optic fibers to go through the tube. All photostimulation experiments were applied at least 4 weeks after viral injection to allow the full expression of channelrhodopsins. All four cagemate mice were habituated to fiber connection for at least 2 days. On the photostimulation day, tube test ranks were first confirmed again without light. In stimulation trials, 473 nm blue light was turned on right before tube entering. A 473 nm blue light was delivered constantly (Kamigaki and Dan, 2017; Yizhar et al., 2011) throughout the test on the PV-Cre and SOM-Cre mice; and delivered at 20 Hz, 5 ms pulse (Pi et al., 2013) on VIP-Cre mice. Light intensity was gradually increased, until the rank changed or the maximal 30mW light intensity was reached. The real range of light intensity that induced rank change was 0.3 - 25 mW for CaMKIIα::ChR2, 2 - 21 mW for PV::ChR2, 1 - 20 mW for VIP::ChR2 and 2 - 21 mW for SOM::ChR2 mice (light intensity measured at fiber tips, Figure S1D). Tube tests before and with light stimulation on the photostimulation day were videotaped for annotation, and the behaviors from light-off and light-on condition of rank changed trials of the same mice were further compared.

Chemogenetic inhibition of dmPFC interneurons in tube test

PV-Cre, VIP-Cre and SOM-Cre mice injected with AAV-DIO-hM4D virus were grouped into 4 with age-matched C57/BL6 mice for the tube test. One transgenic mouse from a cage with stable ranks received i.p. injection of CNO (dissolved in saline, 1 mg/kg for PV::hM4D mice, 5 mg/kg for VIP::hM4D mice and SOM::hM4D mice) and its cagemates were injected with comparable volume of saline. Ranks of the test mice were measured with tube test at 0, 0.5, 1.5, 6, 24, 48 and 72 hours after CNO injection.

Open field test

PV::ChR2 and VIP::ChR2 mice were individually introduced in the center zone of open field (40 × 40 × 40 cm) chambers for 10-minute tests under uniform dim light with a described procedure (Zhou et al., 2017), during which 473 nm blue light was intermittently turned on and off on the test mice with 1min epochs (50 Hz, 5 ms, 20 mW for PV::ChR2 mice; 20 Hz, 5 ms, 20 mW for VIP::ChR2 mice in light-on epochs). The sequence of ON-OFF was switched for different animals to balance the temporal effect. Total distance and percent of time staying in the center zone were analyzed to compare the locomotion and anxiety of mice between light-on and -off epochs.

Immunohistochemistry

Histology was performed to confirm the location of implanted optic fibers. Mice were transcardially perfused under deep anesthesia with 50 mL of phosphate-buffered saline (PBS) followed by 50 mL of 4% w/v paraformaldehyde (PFA). Brains were collected and postfixed in 4% w/v PFA at 4°C for 1 - 2 h, followed by cryoprotection with a 30% w/v sucrose solution for 1-2 days. Dehydrated brains were then sectioned into 40 μm thick coronal slices using a cryostat (Leica Microsystems). Slices were counterstained with Hoechst before imaging with microscope (Nikon A1).

To confirm expression of ChR2 and hM4D in different cell types, immunostaining was performed on mPFC sections of ChR2 or hM4D expressing animals. The antibodies used were rabbit anti-CaMKIIα (ab-52476, Abcam; 1:1000), rabbit anti-PV (PV 27, Swant; 1:5000), rabbit anti-VIP (20077, ImmunoStar; 1:300), rabbit anti-somatostatin (T-4103 Peninsula Laboratories LLC; 1:1000), chicken anti-GFP (ab13970, Abcam; 1:1000), Alexa Fluor 488 goat anti-rabbit IgG, Alexa Fluor 488 goat anti-chicken IgG, Alexa Fluor 546 goat anti-rabbit IgG (all 1:1000, Thermo Fisher Scientific). Slices for checking the injection site were counterstained with Hoechst in the final incubation step. The slides were mounted with 70% glycerin.

Fiber photometry recording

Mice were first trained singly for four days. On the first two days, mice were trained to walk through a 30 cm tube for 10 trials per day. On the next two days, they were trained for 10 trials per day to walk through a modified 60-cm tube with two movable doors (15 cm to one end), where they would wait for a delay period (gradually increased from 0 to 5 s over training trials) before the door open. From Day 5, tube tests were carried out between cagemates in the modified 60 cm tube: two mice were gently released at the ends of tube and waited at the doors for 5 s and then walked to the middle of the tube and started competitions with push or retreat (Figure 3C). The 5 s delay period before gate-lift allowed us to record for clean pre-push/retreat baseline without disruption from human handling. Additionally, only well-trained mice with stable ranks were used for fiber photometry recording. In those cases, low-rank mice usually retreated quickly after high-rank opponents initiated pushes, therefore calcium signals from push and retreat epochs had lower chance to be mixed with fluorescence change induced by other adjacent behaviors like resistance or push back.

Please cite this article in press as: Zhang et al., Dynamics of a disinhibitory prefrontal microcircuit in controlling social competition, Neuron (2021), https://doi.org/10.1016/j.neuron.2021.10.034

The fiber photometry system (Thinker Tech Nanjing Biotech Co., Ltd.) delivers a beam of 488 nm laser light and the GCaMP fluorescence signals were acquired at a sampling rate of 100 Hz. The laser intensity was adjusted to a low level (40 μw) at the tip of optic fiber to minimize bleaching. Behaviors were recorded by a camera set aside of the tube and push and retreat epochs from the recorded mice were manually annotated with the BORIS software . To synchronize the video and fiber photometry recording, an external trigger simultaneously sent a TTL pulse to the data acquisition box and light up an LED light which could be captured by the video camera.

For the peri-event time histograms (PETHs) analysis, the onsets of each behavior were aligned to time zero and the signals were standardized using Z score and binned at 100 ms. Baseline activities were calculated from -3 s to -1 s before each behavioral epoch. When calculating PETH of walking through the tube, Ca^{2+} signals were aligned to the time point when mice arrived at the middle of the tube. Permutation test was applied to analyze the statistical significance of the fluorescence response, as previously reported (Li et al., 2016). We used 1,000 permutations for an α-level of 0.05 to compare the distribution of Z score at each time point to the baseline period. P values were further corrected for multiple comparisons using FDR.

The change latency in Figure 4J is defined as the duration between the onset of behavior and the time when Z score reached the threshold ($Z = \pm 2$, corresponding to $p < 0.05$, Figure S5). The change latency and the decay time are vacant if the Z score does not reach the threshold. The decay time in Figure 4J is defined as the duration between the onset of behavior and the time at which Z score drops back to the threshold ($Z = \pm 2$, corresponding to $p < 0.05$, Figure S4). If decay time exceeds 4 s, we counted it as 4 s.

Acute *in vivo* optrode recording in head-fixed mice

Optrode recording was performed in transgenic mice VIP-Cre::Ai32 and PV-Cre::Ai32, respectively. A stainless-steel head-plate was first cemented with dental acrylic and the silver wires with two screws were attached to the skull as ground. Mice were headfixed to stereotaxic apparatus for 2-hour habituation the day before recording.

On the day of recording, mouse was anesthetized with isoflurane and headfixed in the stereotaxic apparatus. After a craniotomy (0.5-1.0 mm in diameter) was made over the dmPFC, the brain surface was covered by silicone elastomer (Kwik-Sil, WPI) for protection. Then, the anesthesia was stopped. After recovery from the anesthesia for 1-2 hours, the silicone elastomer and dura matter were removed immediately before the insertion of the optrode. The optrode consisted of a 16-channel electrode with a 105 μm core optic-fiber terminated 200 μm above the top recording site (A1 × 16-5 mm-25-177-OCM16LP, NeuroNexus). We dipped the optrode in the DiI (0.2% w/v in the ethanol, Beyotime) before acutely inserting it in the dmPFC (ML, ± 0.4 to 0.6 mm from midline; AP, 2.43 mm from bregma). The optrode was lowered gradually from 1.2 mm to 1.6 mm to record units at different Z axis locations, which were verified by DiI-labeled electrode track at the end of the experiment (Figure S8).

Wide band electronic signals (0.05-8000 Hz) were sampled at 40 kHz with gain of 5000 × by OmniPlex Neural Data Acquisition System (Plexon Inc). Spontaneous spiking signals were band-pass filtered between 300 and 8000 Hz. Common median reference (CMR) was assigned as a digital reference. In order to examine the activation of one subtype of inhibitory neurons (PV or VIP) on spontaneous dmPFC dynamics, we applied 10 s constant blue light (470 nm, 2 mW at fiber tip, constant, 20 repetitions) on PV-Cre::Ai32 mice and 1 s blue light pulses (470 nm, 10 mW at fiber tip, 20 Hz, 5 ms, 60 repetitions) on VIP-Cre::Ai32 mice, respectively. For optical identification of PV and VIP neurons, blue light pulses (470 nm, 10 mW at fiber tip, 1 Hz, 1 ms, 180 repetitions) were delivered at the start and end of each recording session.

For recording with opto-inhibition of PV neurons, we applied yellow light (589 nm, 8 mW at fiber tip, 1 Hz, 10 ms, 180 pulses) on PV::eNpHR3.0 mice.

Chronic *in vivo* optrode recording on PV-Cre::ChR2 mice

Single-unit recording was performed as previously described (Hua et al., 2018; Tseng et al., 2011; Zhou et al., 2017). Briefly, a homemade adjustable optrode was constructed with 16 single electrodes (STABLOHM 650, California fine wire) and an optic fiber (25 mm length, Inper Inc.). PV-Cre::Ai32 mice were implanted with optrodes targeting the dmPFC (ML, 0.5 mm; AP, 2.43mm from bregma; DV, −1.2 mm from the brain surface). Silver wires with two screws were attached to the skull as ground. The procedure of surgery was similar to optical fiber implantation (see above)

Mice were single housed for 7 days for recovery after surgery. Mice were then trained daily in tube test wearing sham wire to get habituated with the recording procedure. During recording, optrode of one mouse was connected to the amplifier whereas optrode of the other mouse was connected to a sham wire. Video recording was also conducted simultaneously with electrophysiology recording to get a side view of the tube at 25 frames per second. To synchronize the video and electrophysiology recording, we used Fiber Optogenetics System (Inper Inc.) to simultaneously delivery a light pulse to the video and an electrical pulse to the recording setup. The optrodes were lowered gradually by 62 μm to record units of different Z axis locations.

For optical identification of PV INs, blue light pulses (470 nm, 1 ms duration, 5 mW at fiber tip) were delivered at the end of each recording session with different frequencies (1Hz, 10Hz and 20 Hz).

Videos of every tube test trial were analyzed frame by frame. Behavior epochs during the entire tube test were marked using the BORIS software. Then, we aligned the behavior epochs with electrophysiology data.

Please cite this article in press as: Zhang et al., Dynamics of a disinhibitory prefrontal microcircuit in controlling social competition, Neuron (2021), https://doi.org/10.1016/j.neuron.2021.10.034

Spike sorting and unit classification with optogenetic tagging

Spike waveforms were identified by threshold crossing and sorted into units (presumptive neurons) by principal component analysis (PCA) using the Offline Spike Sorter (Plexon). We excluded the spikes with inter-spike intervals (ISIs) less than the refractory period (1.4 ms). Cross-correlation histograms were plotted to ensure that no unit was discriminated more than once on each recording site. Neurons with a signal-to-noise ratio < 2 and baseline firing rate < 1 Hz were excluded from further analysis.

All units were further classified as the WS, NS-nonFSI and FSI based on the peak-trough distance and the baseline firing rate. A unit was classified as WS neuron if its peak-trough distance was > 400 μs, or as a NS neuron if its peak-trough distance was ≤ 400 μs. NS neurons with firing rate > 8 Hz were classified as FSI (Kim et al., 2016; Varga et al., 2012).

The opto-tagged neurons were identified based on short spike latency (< 5 ms), low jitter (< 3 ms), and a significant change ($p < 0.001$) in spike timing relative to the onset of laser stimuli (stimuli-associated spike latency test, SALT) (Kvitsiani et al., 2013). The tagged PV neurons have a 3.61 ± 0.50 ms latency and a 1.43 ± 0.30 ms jitter. The tagged VIP neurons have a 0.90 ± 0.28 ms latency and a 0.011 ± 0.0009 ms jitter. We also adopted the Pearson's correlation coefficient (r) to compare the waveforms of units recorded before and during the laser stimulation, and only those units showing no substantial changes ($r > 0.9$) in their waveforms were included in further data analysis.

Unit firing analysis

Data analysis was performed using custom-written MATLAB program (MathWorks). In recordings with PV/VIP activation, the PSTH was estimated by convolving the raster plot with a doubly adaptive Gaussian kernel, and then standardized to report the light-induced neuronal response (Pi et al., 2013). Mean and standard deviation of baseline activity were calculated and used to generate Z score. The baseline period is a stimulus-free period before the light pulses. To detect light-induced changes of firing rate, the Z score of the whole light on epoch for the PV activation in Figures 6E–6G and the VIP 20 Hz activation in Figures 7K–7M, or 10-30 ms after the light onset for the transient PV inhibition in Figure S10 were compared to an equivalent baseline period using a Wilcoxon signed-rank test. For the three separated neural responses to VIP activation, the direct inhibition (Inh) neurons are defined as those with a significant decrease of firing rate in the first phase (0-10 ms) compared to the baseline activities. The inhibition-activation (Inh-act) neurons had an initial decrease in firing rate as the Inh group, followed by a significant increase of firing rate in the second phase (30-45 ms) compared to the baseline activities. The delayed activation (dAct) neurons are those with a significant increase of firing rate without the initial inhibition.

In the recordings during tube test trials of PV-Cre::ChR2 mice, mean firing rate around onsets of push or retreat epochs (-0.5 to 0.5 s from onset) were used to be compared with mean basal firing rate (-3 to -1.5 s from onset) with the paired Wilcoxon signed-rank test for each identified WS, putative PV, and NS neurons. For the identification of the first time point of significantly change, a moving 20 ms analysis window was used to examine the effect of excitation or inhibition compare to the -3 to -1.5 s as the baseline period. Inhibited or activated neurons are classified according to the first time point of significantly change. P values were further corrected for multiple comparisons using FDR.

Miniature two-photon imaging and optogenetic experiments

For miniature two-photon experiments, 400 nL mixture virus of $AAV_{2/9}$-hSyn-GCaMP6f (titer: 3.4×10^{12}, Taitool) and $AAV_{2/9}$-EF1a-Flex-JAWs-tdTomato-ER2 (titer: 4.2×10^{12}, Taitool)-were injected into the dmPFC. Following viral injection, a 1 mm diameter, ~4 mm length gradient refractive index lens (GRIN lens; Go!Foton) was slowly advanced into the dmPFC until the tip was placed at DV: −1.10 for PV-Cre mice. But for VIP-Cre mice, the coordinates (angle: 14°, ML: 0.71 from midline, AP: 2.43 from bregma, DV: 1.2 from dura) were used to target the superficial-layer-located VIP neurons. After 3-4 weeks of viral expression, an imaging baseplate was positioned over the GRIN lens and cemented with dental acrylic. The miniature two-photon microscope (FHIRM-TPM V2.0, Field of view: 420 × 420 μm^2; Resolution: ~1.13 μm; working distance: 1 mm) was detachable while its holder was mounted permanently onto a baseplate over the GRIN lens. The cover of the holder and protective glue (Kwik-Cast, WPI Inc, USA) on the GRIN lens were removed before imaging. Then headpiece was mounted on the holder and locked with M2 screws. Imaging data was acquired using the imaging software (GINKGO-MTPM, Transcend Vivoscope Biotech Co., Ltd, China) at a frame rate of 10 Hz (512 × 512 pixels) with a femtosecond fiber laser (~35 mW at the objective, TVS-FL-01, Transcend Vivoscope Biotech Co., Ltd, China). GCaMP6f was excited at 920 nm and tdTomato was excited at 1,030 nm. tdTomato images were collected before each imaging session. For combined imaging and optogenetic experiments, femtosecond laser (920 nm) for calcium imaging and red light (635 nm laser, MRL-III-635L, New Industries Optoelectronics Tech. Co., Ltd, China) for inhibition of cellular activity with JAWs were transmitted through the microscope objective and implanted GRIN lens. The red light was transmitted through the soft fiber buddle, which was also used to collect the fluorescence, and customized miniature objective lens (NA: 0.5, WD: 1 mm). The fluorescent signal and the red light were separated by a dichroic mirror (FF562-Di03-25x36, Semrock Inc., USA). The output power of the red light can be controlled by adjusting the laser driver (~5 mW at the objective). The stimulation protocol was set by the imaging software. The red light stimulation was started after 1800 frames baseline imaging of each experiment, then turned on for 200 frames, and then turned off for 600 frames, with 10 repetitions. A 520/30 filter (FF01-525/30, Semrock Inc., USA) was used for GCaMP6f imaging and optogenetic experiments, and a 605/52 nm filter (ET605/52-M, Chroma Inc., USA) was used for tdTomato imaging. Timestamps of imaging frames were marked according to the controller (TVS-MMM-01, Transcend Vivoscope Biotech Co., Ltd, China)

Please cite this article in press as: Zhang et al., Dynamics of a disinhibitory prefrontal microcircuit in controlling social competition, Neuron (2021), https://doi.org/10.1016/j.neuron.2021.10.034

Analysis of two-photon calcium imaging data

The piecewise rigid motion correction NoRMCorre (Pnevmatikakis and Giovannucci, 2017) was first used to eliminate the slight x-y motion of the field of view caused by the mouse movement. The active cellular regions of interest (ROIs) were identified by STNeuroNet (Soltanian-Zadeh et al., 2019) in both red and green channels and manually corrected in ImageJ (NIH). Finally, the identified cellular ROIs in red and green channels were matched based on centroid position. Further, we performed the calcium signal extraction according to the commonly used processing strategy called Annular Ring Subtraction (ARS) method (Chen et al., 2013; Kerlin et al., 2010; Pinto and Dan, 2015). Relative changes in calcium fluorescence were calculated using the Z score in MATLAB. Transients were detected post hoc using a threshold of 4 times the standard deviation of the full signal. To define responsive cells, the average of time-binned Ca^{2+} signals were compared between the stimulus and equivalent baseline period using a Wilcoxon signed-rank test with a significance threshold of $p < 0.05$.

QUANTIFICATION AND STATISTICAL ANALYSIS

All data are shown as mean ± SEM unless otherwise specified. Statistical analyses were done with Prism 8.1 (GraphPad) or MATLAB. Comparisons were conducted with Student's t test to compare Gaussian distributions while Mann-Whitney tests were used for non-Gaussian distributions. Two-way ANOVA with repeated-measures followed by Bonferroni's post-tests for multiple comparisons where appropriate. Results were considered statistically significant when the P value < 0.05. More details are provided in the Table S1.

Neuron, Volume *110*

Supplemental information

Dynamics of a disinhibitory prefrontal microcircuit in controlling social competition

Chaoyi Zhang, Hong Zhu, Zheyi Ni, Qiuhong Xin, Tingting Zhou, Runlong Wu, Guangping Gao, Zhihua Gao, Huan Ma, Haohong Li, Miao He, Jue Zhang, Heping Cheng, and Hailan Hu

Supplementary Figures

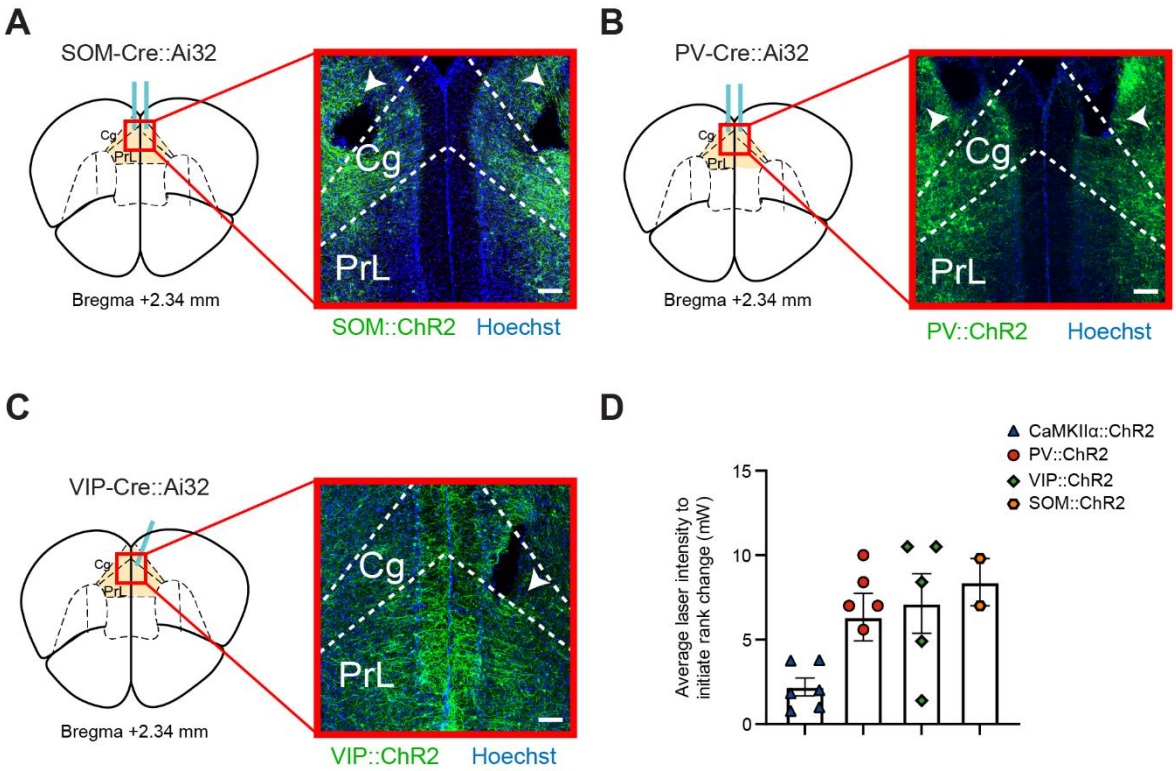

Figure S1. Viral targeting, fiber placement and average laser intensity used for cell-type-specific optogenetic stimulation, related to Figure 1

(A, B and C) Schematics illustrating the optical fiber placement (indicated by the white arrowhead) in the dmPFC of SOM::Ai32 (A), PV::Ai32 (B) and VIP::Ai32 (C) mice. Scale bar, 100 μm.

(D) Average laser intensity used to induce rank change in individual mice. Error bars indicate ± SEM.

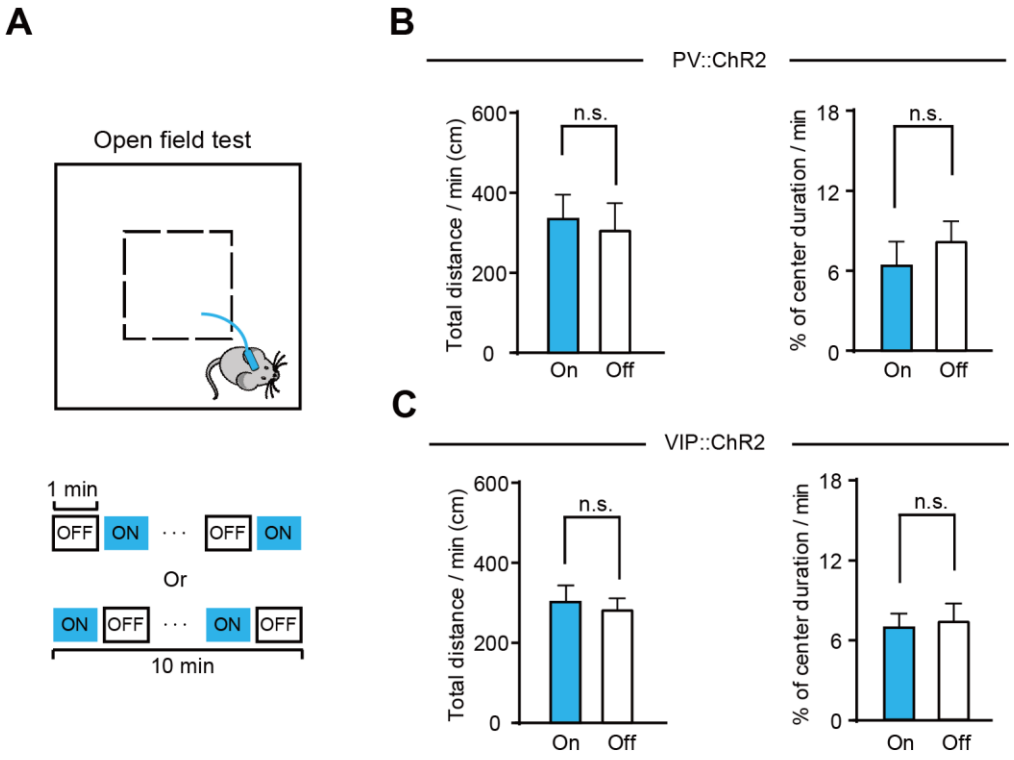

Figure S2. Photoactivation of dmPFC PV or VIP neurons does not change locomotion and anxiety, related to Figure 1

(A) Schematic of open field test (OFT) and intermittent photostimulation protocol.

(B) Mean total distance (Left) and percentage of center duration (Right) per minute in light on and off epochs across 10 min OFT while photostimulating PV neurons. n = 8 mice. Paired t-test. Error bars indicate ± SEM.

(C) Mean total distance (Left) and percentage of center duration (Right) per minute in light on and off epochs across 10 min OFT while photostimulating VIP neurons. n = 8 mice. Paired t-test. Error bars indicate ± SEM.

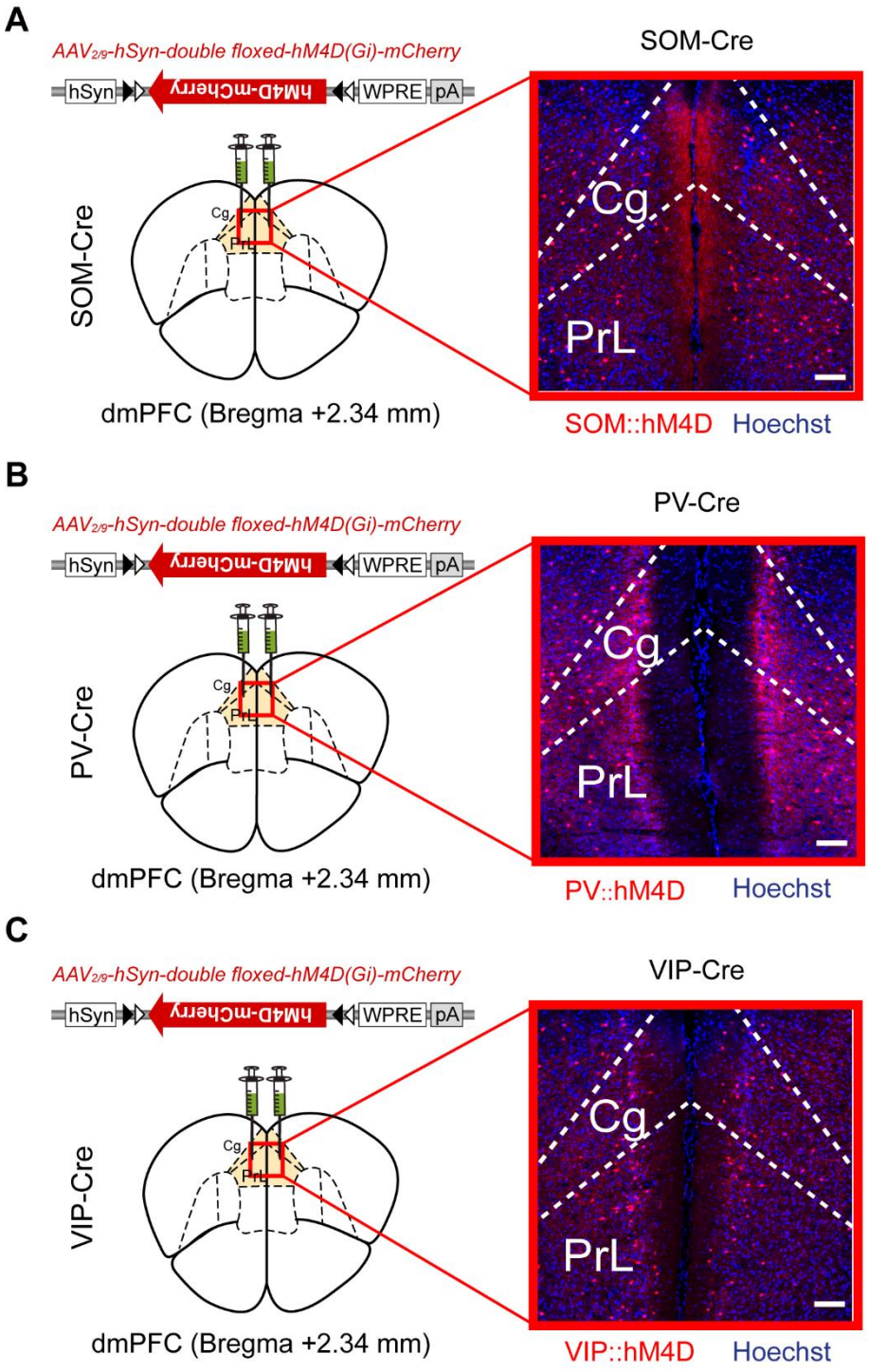

Figure S3. Viral targeting in the dmPFC for cell-type-specific chemogenetic inhibition experiments, related to Figure 2

(A, B and C) Schematics illustrating the viral construct, viral injection site and viral expression in the SOM-Cre (A), PV-Cre (B) and VIP-Cre mice (C). Scale bar, 100 μm.

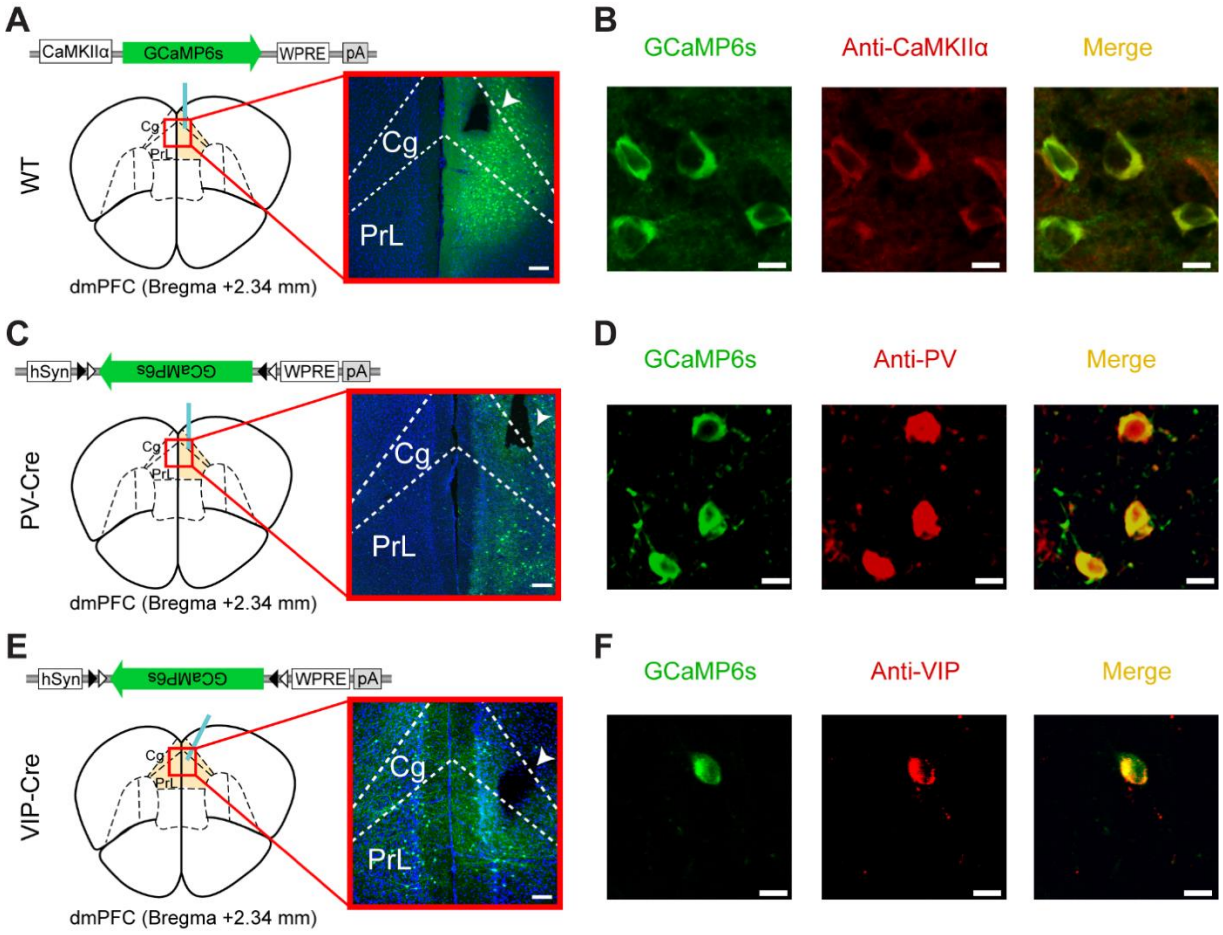

Figure S4. Characterization of cell-type specific GCaMP6 expression for fiber photometry experiments, related to Figure 4

(A, C and E) Schematics illustrating viral construct, viral injection site and optic fiber placement in the wild type (WT) (A), PV-Cre (C) and VIP-Cre (E) mice. White arrowheads indicate the fiber placement sites in the dmPFC. Scale bar, 100 μm.

(B, D and F) Immunostaining confirming the specificity of GCaMP6s expression in the PYR (B), PV (D) and VIP (F) neurons. Scale bar, 10 μm.

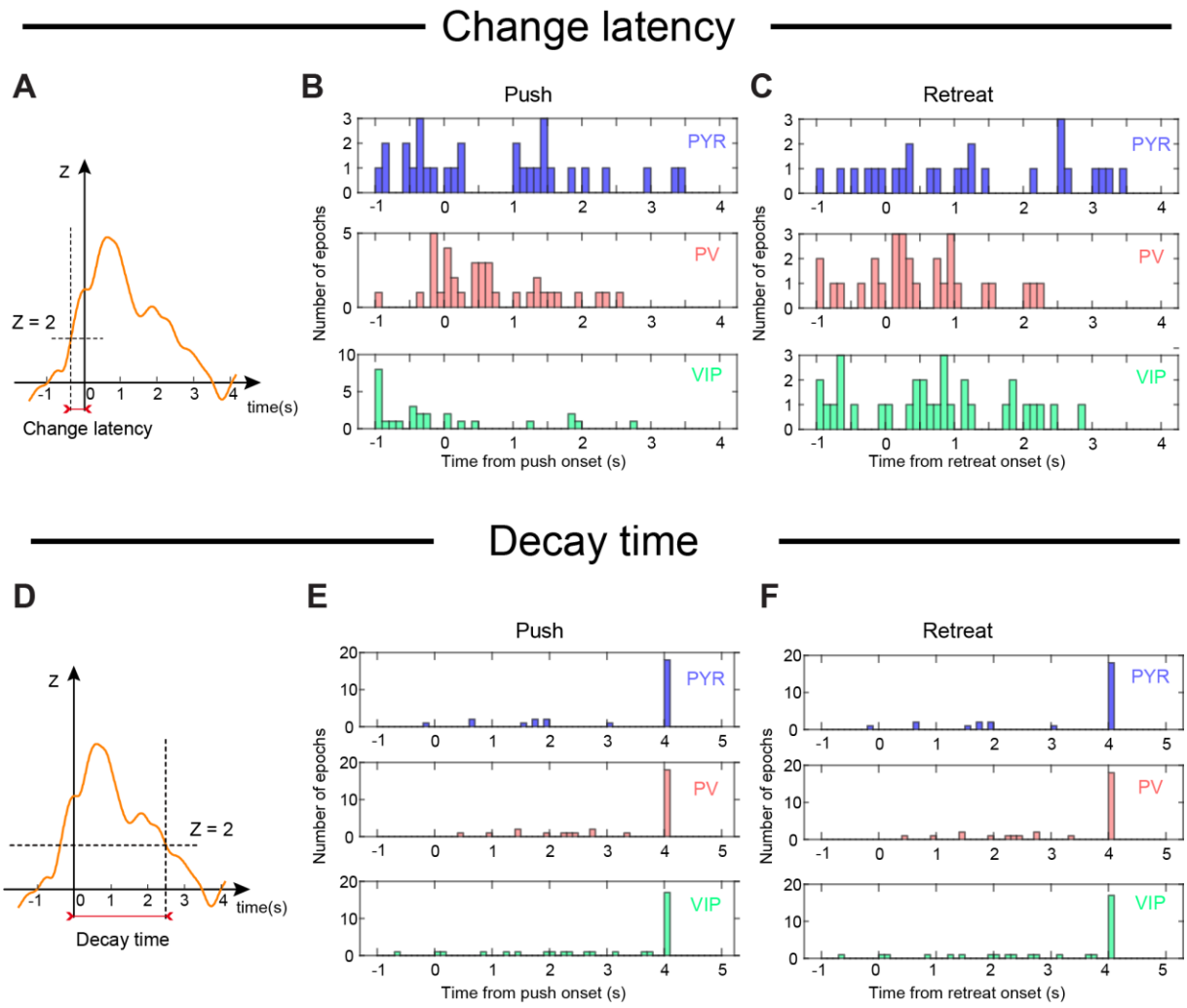

Figure S5. Definition and distribution of change latency and decay time of Ca^{2+} signals, related to Figure 4

(A and D) Illustration of the definition of change latency (A) and decay time (D). A sample trace of Z-scored Ca^{2+} signals of VIP neurons during push is shown. The vertical and horizontal dashed lines indicate the time and Z-score when Ca^{2+} signal reaches the threshold ($Z = \pm 2$, corresponding to $p < 0.05$) (A) or returns to the threshold ($Z = \pm 2$) (D), respectively. Red double-headed arrows annotate the change latency (A) and decay time (D). If the Z-score does not reach the threshold, the change latency and decay time are not calculated. If decay time exceeds 4s, it is counted as 4 s.

(B and C) Distribution of Ca^{2+} signal change latency of PYR (top), PV (middle), and VIP (bottom) neurons in push (B) and retreat (C) epochs.

(E and F) Distribution of Ca^{2+} signal decay time of PYR (top), PV (middle), and VIP (bottom) in push (E) and retreat (F) epochs.

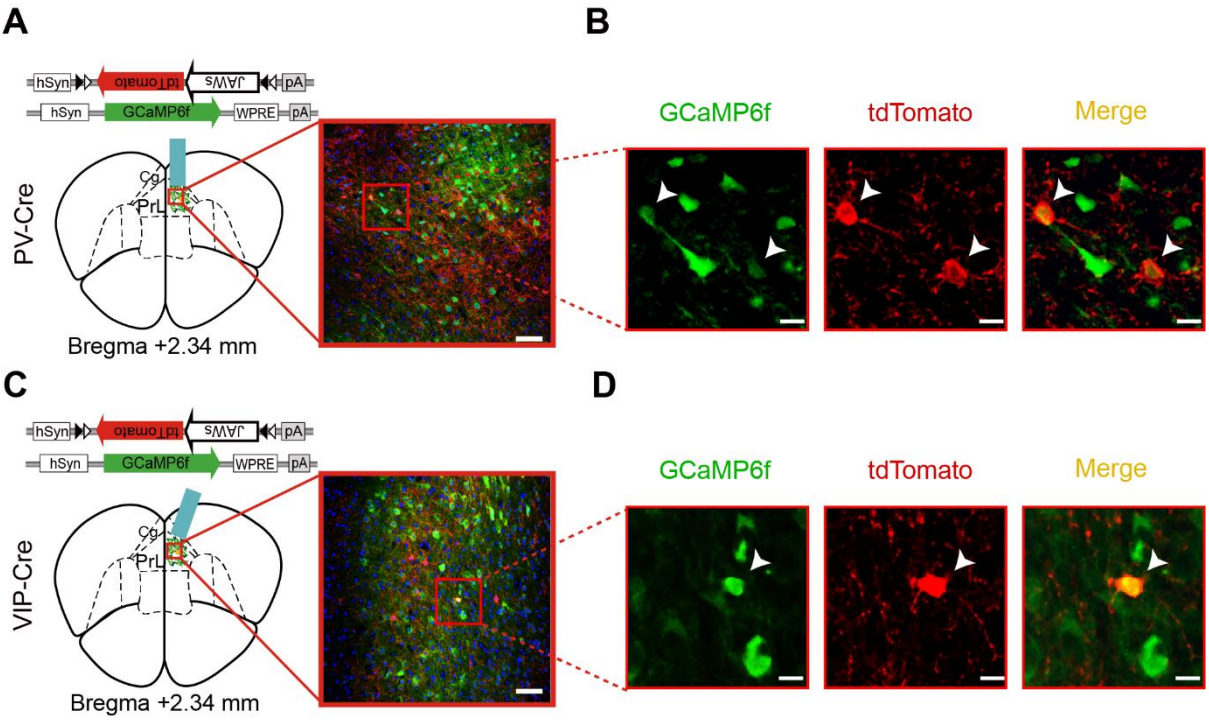

Figure S6. Expression of GCaMP6f and JAWs for miniature two-photon microscopic recording, related to Figure 5

(A and C) Schematics illustrating the viral constructs and lens implantation sites in the dmPFC of PV-Cre (A) and VIP-Cre (C) mice. Scale bar, 50 μm.

(B and D) Immunostaining showing the colocalization of GCaMP6f and JAWs-tdTomato (indicated by the white arrowheads) in PV-Cre (B) and VIP-Cre (D) mice. Scale bar, 10 μm.

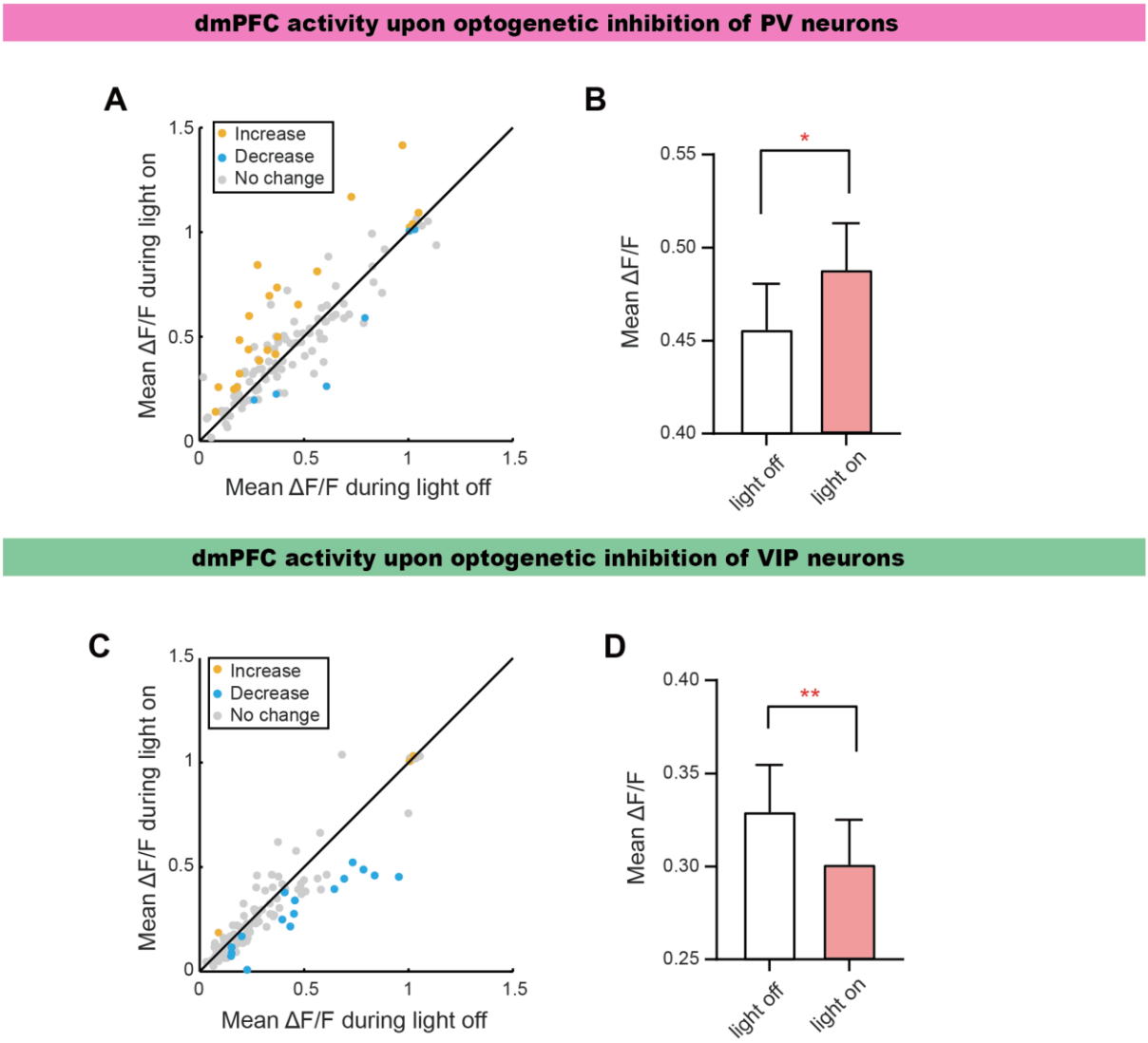

Figure S7. dmPFC Ca^{2+} signal changes upon inhibition of PV and VIP neurons, related to Figure 5

(A and C) Scatter plots of the fluorescence signal (ΔF/F) of all non-PV neurons (n=154) from PV::JAWs mice (A) and non-VIP neuron (n=123) from VIP::JAWs mice (C) during light on epochs, plotted against fluorescent signal (ΔF/F) during light off epochs. Each dot represents the mean from a single cell. Colored circles indicate neurons that showed significant increase (orange) or decrease (blue) of Ca^{2+} signal (Wilcoxon matched-pairs signed rank test, $p < 0.05$).

(B and D) Mean fluorescence signal (ΔF/F) of all non-PV neurons (n=154) and non-VIP neuron (n=123) upon optogenetic inhibition of PV (B) and VIP (D) neurons. Wilcoxon matched-pairs signed rank test.

Error bars indicate ± SEM, * $p < 0.05$; **$p < 0.01$.

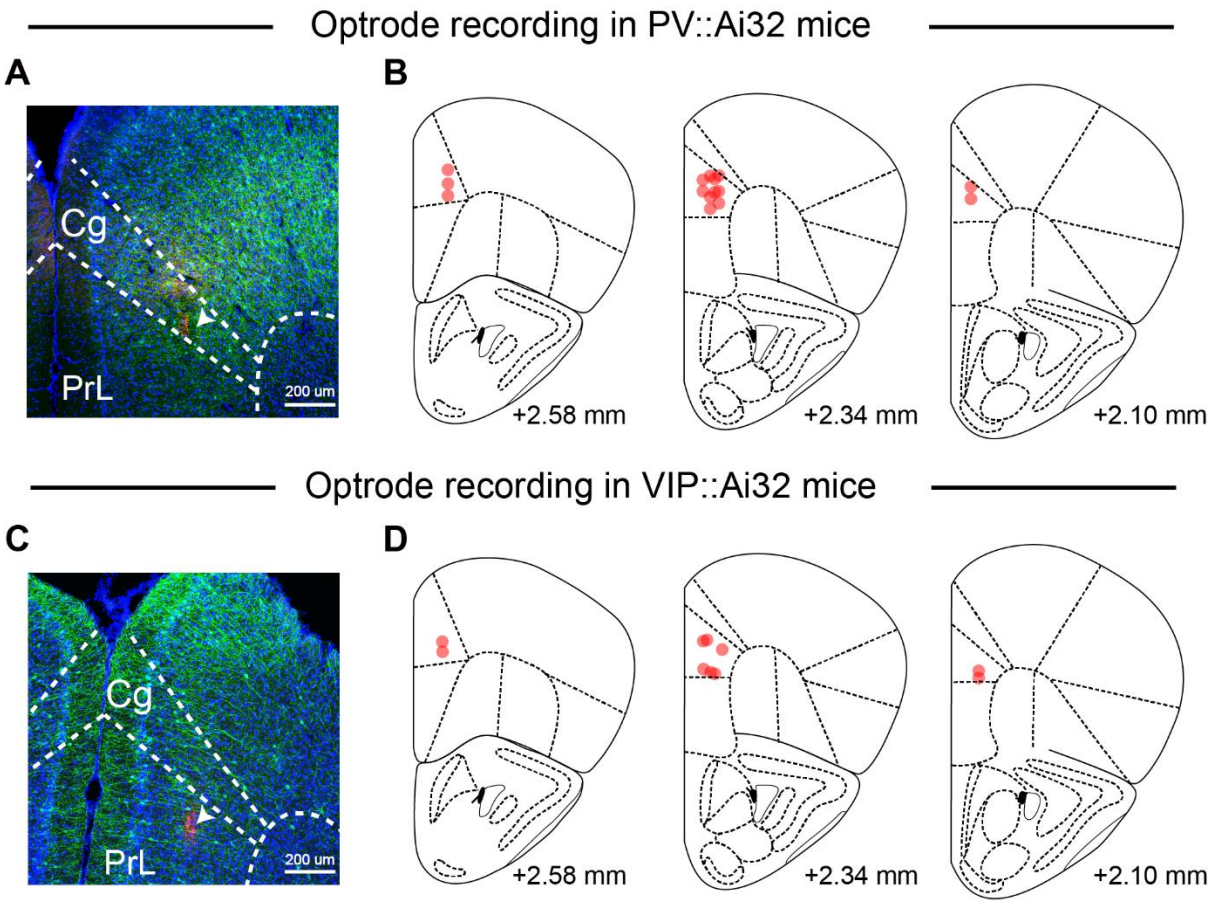

Figure S8. Optrode placement in dmPFC for optrode recording experiments, related to Figures 6 and 7

(A and C) Brain slices from a representative PV::Ai32 (A) and VIP::Ai32 (C) mouse with an optrode implanted in the dmPFC. Arrows indicates optrode track marked with a red fluorescent dye Dil. Cg: cingulate cortex; PrL, prelimbic cortex; Dashed white lines are boundaries of subregions; Blue, Hoechst. Red, Dil. Scale bar, 200 μm. (B and D) Location of optrode tips in all recorded PV::Ai32 (B) and VIP::Ai32 (D) mice.

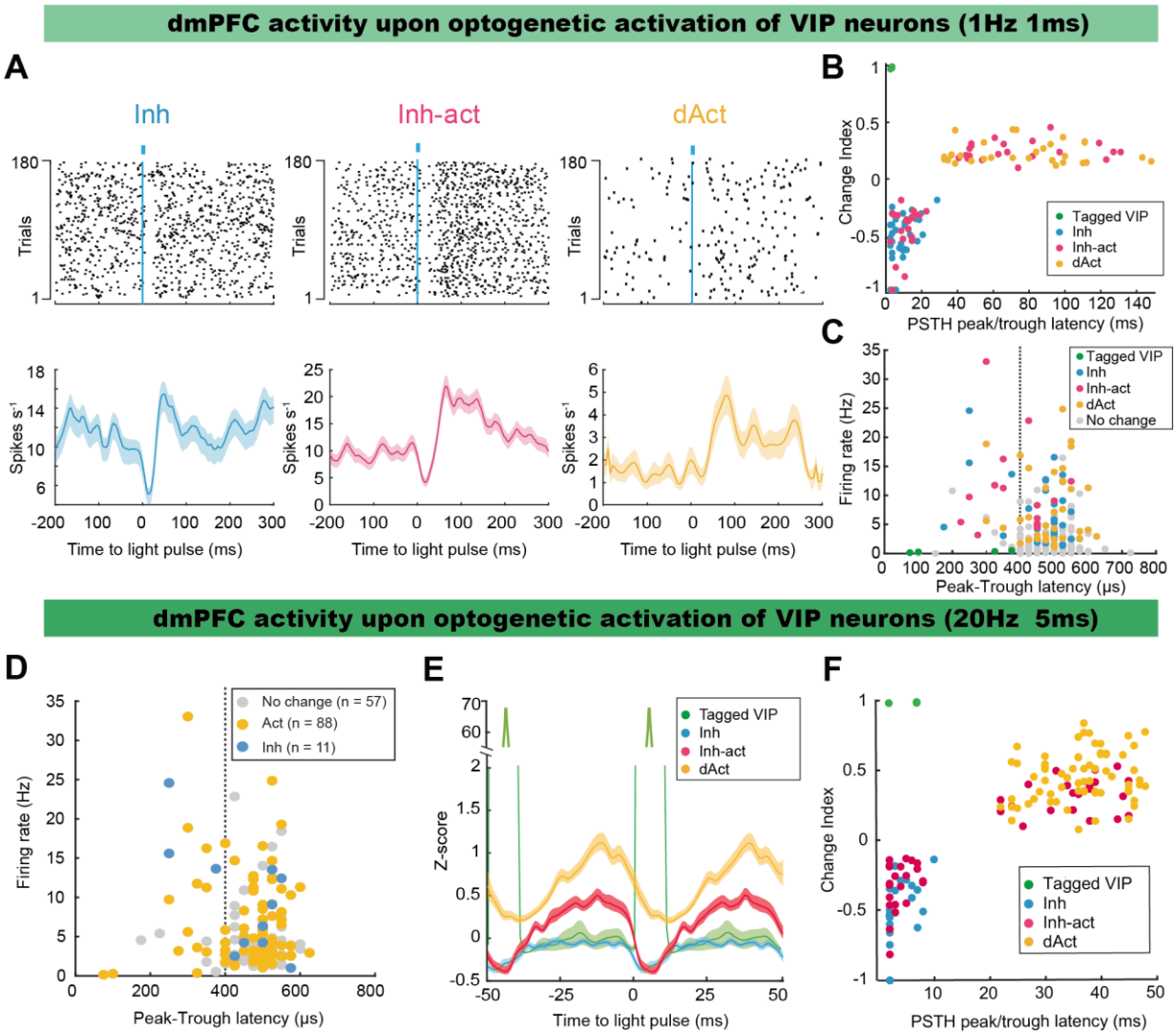

Figure S9. dmPFC response upon distinct VIP stimulation protocol, related to Figure 7

(A) Raster plot (top) and PSTH (bottom) of representative neurons in the Inh (left), Inh-act (middle) and dAct (right) groups when VIP neurons were stimulated with the 1 Hz protocol. Shaded areas define ± SEM.

(B) Change index during the 1 Hz VIP stimulation plotted against PSTH peak/trough latency of four separated clusters of significantly modulated neurons: tagged VIP (green), Inh (blue), Inh-act (magenta) and dAct (orange). Change index is defined as firing rates (light on - light off) / (light on + light off), such that a value > 0 means activation, and a value < 0 means inhibition, of spiking during light on.

(C) Baseline firing rate plotted against peak-to-trough latency of tagged VIP (green), Inh (blue), Inh-act (magenta), dAct (orange) and No change (grey) neuron groups when VIP neurons were stimulated with the 1 Hz protocol.

(D) Baseline firing rate plotted against peak-to-trough latency of all recorded units when VIP neurons were stimulated with the 20 Hz protocol. Colored circles indicate neurons that showed differences in firing rates during 1s light on versus 1s light off. Gray, no change; yellow, activated; blue, inhibited.

(E) Temporal expansion of the PSTHs of tagged VIP (green), Inh (blue), Inh-act (magenta) and dAct (orange) neurons in the 1s (20 Hz, 5 ms) protocol. Shaded areas define ± SEM.

(F) Change index during the 20 Hz VIP stimulation plotted against latency of PSTH peak/trough latency of four separated clusters of significantly modulated neurons.

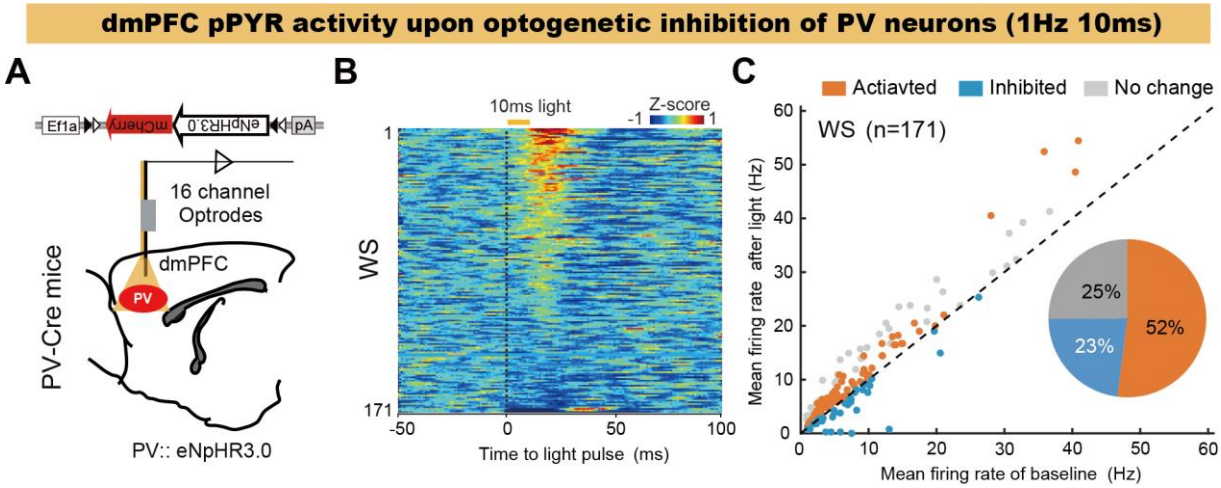

Figure S10. Transient inhibition of PV neurons induces transient activation of putative pyramidal neurons in dmPFC, related to Figure 7

(A) Schematic illustration of in vivo optrode recording in PV-Cre mice expressing DIO-eNpHR3.0-mCherry virus in the dmPFC.

(B) PSTHs of Z-scored firing rate from all recorded WS (wide-spike) neurons.

(C) Scatter plots of the mean firing rates of WS neurons before (at -50-0 ms) the 10 ms light on epoch, plotted against firing rates after (at 10-30 ms) the light on epoch. Colored circles indicate neurons that showed significant light-induced firing rate increase (orange) or decrease (blue). Inset pie graphs show the percentage of neurons that are significantly inhibited (blue), activated (orange), or unchanged (gray) after the light stimulation.

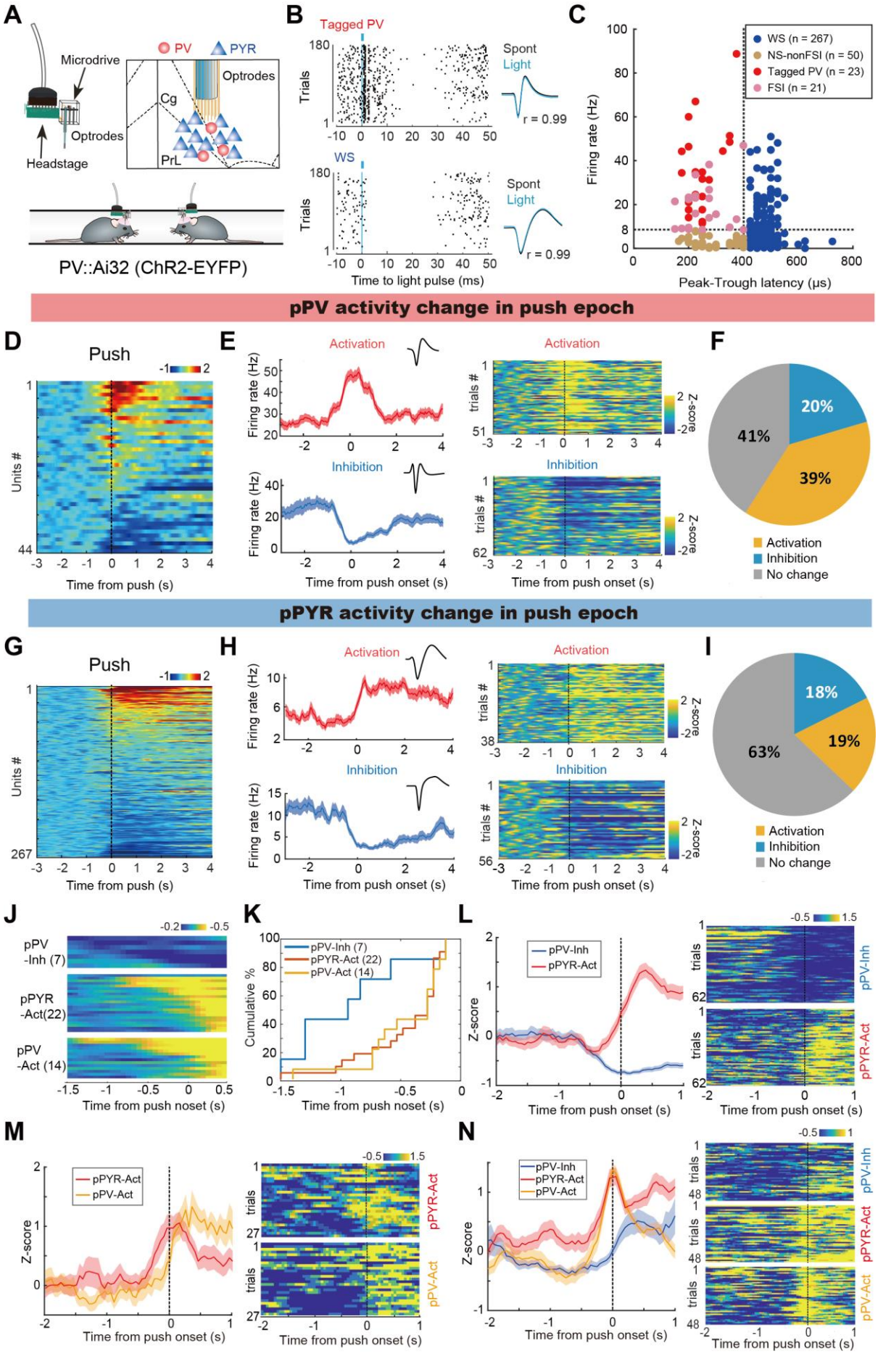
A
Microdrive
Optrodes
Headstage
PV
PYR
Optrodes
Cg
PrL
PV::Ai32 (ChR2-EYFP)
B
Tagged PV
Trials
Spont
Light
r = 0.99
WS
Time to light pulse (ms)
C
WS (n = 267)
NS-nonFSI (n = 50)
Tagged PV (n = 23)
FSI (n = 21)
Firing rate (Hz)
Peak-Trough latency (μs)
pPV activity change in push epoch
D
Push
Units #
Time from push (s)
E
Activation
Inhibition
Firing rate (Hz)
trials #
Z-score
Time from push onset (s)
F
20%
41%
39%
Activation
Inhibition
No change
pPYR activity change in push epoch
G
Push
Units #
Time from push (s)
H
Activation
Inhibition
Firing rate (Hz)
trials #
Z-score
Time from push onset (s)
I
18%
19%
63%
Activation
Inhibition
No change
J
pPV
-Inh (7)
pPYR
-Act(22)
pPV
-Act (14)
Time from push noset (s)
K
pPV-Inh (7)
pPYR-Act (22)
pPV-Act (14)
Cumulative %
Time from push noset (s)
L
pPV-Inh
pPYR-Act
Z-score
trials
Time from push onset (s)
M
pPYR-Act
pPV-Act
Z-score
trials
Time from push onset (s)
N
pPV-Inh
pPYR-Act
pPV-Act
Z-score
trials
Time from push onset (s)

Figure S11. Dynamic response of PV and PYR neurons during push in the tube tests, related to Figure 4

(A) Schematic illustration of *in vivo* recording in layer V/VI of dmPFC of behaving PV::ChR2 mice with the movable 16-channel optrodes.

(B) Left: Raster plot of a representative opto-tagged PV (top) and a WS (wide-spike, bottom) neuron recorded from the same electrode. Right: light-evoked spike waveforms (blue) of PV neuron (top) and WS neuron (bottom) were similar to spontaneous ones (black). Pearson's correlation, top: r = 0.99; bottom: r = 0.99.

(C) Baseline firing rate versus peak-to-trough latency of tagged PV (red), WS (blue), NS-nonFSI (narrow spike non-fast spiking interneuron, brown) and FSI (fast-spiking interneuron, pink) neurons.

(D and G) Heatmap of Z-scored firing rate changes from all recorded pPV neurons (D, n = 44 units from 10 mice) and pPYR neurons (G, n= 267 units from 10 mice) aligned to the onset of push bouts.

(E and H) Activities of two example pPV (E) and pPYR (H) units, the top is excited in push bouts and the bottom is inhibited in push bouts. Left, peri-event plots of pPV units firing rate aligned to the onset of push bouts. Mean ± SEM. Inserted: waveforms of two example pPV units. Right, peri-event heatmaps of Z-scored firing rate aligned to onset of push bouts. Each line represents one trial.

(F and I) Percentage of pPV (F) and pPYR (I) neurons exhibiting statistically significant changes in firing rate (See STAR Methods) during push onset.

(J) Z-scored firing rate of push-inhibited pPV (pPV-Inh), push-excited pPV (pPV-Act) and push-excited pPYR (pPYR-Act) neurons sorted by their first significant change time point.

(K) Cumulative distribution of the first significant change time of the pPV-Inh, pPV-Act and pPYR-Act neurons around push onset (pPV-Inh vs pPYR-Act, P = 0.03; pPV-Inh vs pPV-Act, P = 0.02; pPV-Act vs pPYR-Act, P = 0.63; Kolmogorov-Smirnov two-sample test).

(L, M and N) Activities of a pair of pPV-Inh and pPYR-Act neurons (L), a pair of pPYR-Act and pPV-Act neurons (M) and a trio of pPV-Inh, a pPYR-Act and pPV-Act neurons (N) recorded from three recording sites during push epochs. Left, peri-event plots of Z-scored firing rate aligned to the onset of push bouts. Mean ± SEM. Right, peri-event heatmaps of Z-scored firing rate aligned to onset of push bouts. Each line represents firing from one behavioral trial. Note that inhibition onset of the pPV-Inb starts earlier than the excitation onset of pPYR-Act neuron in (L); and that there is a trend of transient inhibition (p = 0.054) of example pPV-Act neuron before push onset in (N).

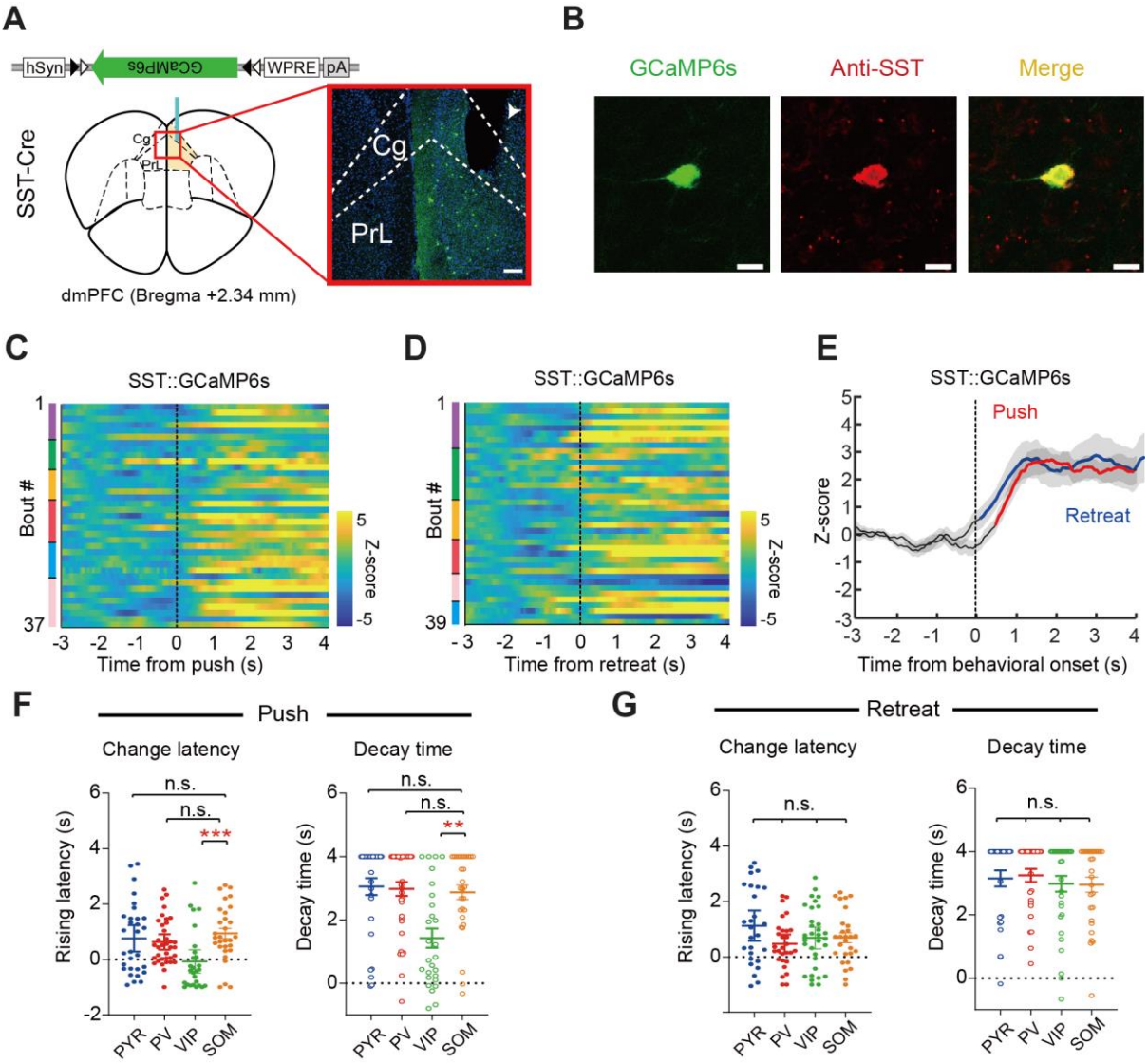

Figure S12. Ca^{2+} activity of dmPFC SOM neurons during effortful and passive behaviors in the tube test, related to Figure 4

(A) Schematic illustrating the hSyn-DIO-GCaMP6s viral construct, viral injection site and optic fiber placement in SST-Cre mouse. Scale bar, 100 μm.

(B) Immunostaining confirming the specificity of GCaMP6s expression in the SST neurons. Scale bar, 10 μm.

(C and D) Heatmap of Z-scored Ca^{2+} signals from dmPFC SST neurons aligned to the onset of push (C, n = 37 trials from 6 mice) and retreat (D, n = 39 trials from 6 mice) bouts. Color bars on the left represent different individual mice.

(E) Peri-event plots of Z-scored Ca^{2+} signal changes from SST neurons during push (red) and retreat (blue) epochs. Solid lines indicate mean and shaded areas indicate ± SEM. Colored thick line segments indicate statistically significant fluorescence change from the baseline in push (red) and retreat (blue) epochs ($p < 0.05$; permutation test).

(F) Latency to significant change (left) and decay time (right) of Ca^{2+} signals in push bouts. Mann-Whitney U-test.

(G) Latency to significant change (left) and decay time (right) of Ca^{2+} signals in retreat bouts. Mann-Whitney U-test. Error bars indicate ± SEM, *$p < 0.05$; **$p < 0.01$; ***$p < 0.001$; n.s., not significant.

Supplementary Table 1. Detailed statistical information

Figure	Sample	Sample size	Statistic method	Statistic results
1D	(Push-initiated) CaMKII α::ChR2 light off vs light on	n = 5, 9	Mann-Whitney U-test	U = 4, p = 0.01
	(Push duration) CaMKII α::ChR2 light off vs light on	n = 5, 9	Mann-Whitney U-test	U = 4, p = 0.0036
	(%Resistance) CaMKII α::ChR2 light off vs light on	n = 5, 9	Mann-Whitney U-test	U = 6.5, p = 0.0245
	(%Retreat) CaMKIIα::ChR2 light off vs light on	n = 5, 9	Mann-Whitney U-test	U = 6.5, p = 0.0245
1G	SOM light on compare with -1 day	n = 8	Wilcoxon matched-pairs signed rank test	W = -3, p = 0.25
1J	PV::ChR2 vs PV::EYFP	n = 10, 6	Two-way repeated measure ANOVA; Bonferroni multiple comparisons post hoc tests.	Day0, p = 0.0042
1K	(Push-initiated) PV::ChR2 light off vs light on	n =5, 12	Mann-Whitney U-test	U = 20, p = 0.3260
	(Push duration) PV::ChR2 light off vs light on	n = 5, 12	Mann-Whitney U-test	U = 6, p = 0.0081
	(%Resistance) PV::ChR2 light off vs light on	n = 5, 12	Mann-Whitney U-test	U = 0, p = 0.0003
	(%Retreat) PV::ChR2 light off vs light on	n = 5, 12	Mann-Whitney U-test	U = 0, p = 0.0003
1N	VIP::ChR2 vs VIP::EYFP	n = 9, 6	Two-way repeated measure ANOVA; Bonferroni multiple comparisons post hoc tests.	Day 0, p = 0.0366
1O	(Push-initiated) VIP::ChR2 light off vs light on	n = 5, 12	Mann-Whitney U-test	U = 9, p = 0.0271
	(Push duration) VIP::ChR2 light off vs light on	n = 5, 12	Mann-Whitney U-test	U = 7.5, p = 0.0139
	(%Resistance) VIP::ChR2 light off vs light on	n = 5, 9	Mann-Whitney U-test	U = 2, p = 0.0015
	(%Retreat) VIP::ChR2 light off vs light on	n = 5, 9	Mann-Whitney U-test	U = 2, p = 0.0015
2D	SOM::hM4D(CNO) vs SOM::hM4D(saline)	n = 8, 8	Two-way repeated measure ANOVA; Bonferroni multiple comparisons post hoc tests.	Day0, all p>0.999
2G	PV::hM4D(CNO) vs PV::hM4D(saline)	n = 7, 6	Two-way repeated measure ANOVA; Bonferroni multiple comparisons post hoc tests.	0.5h (p = 0.0066); 1.5h (p = 0.04); 6h (p = 0.04)
2H	(Push number) PV::hM4D CNO vs before	n = 8, 17	Mann-Whitney U-test	U = 30, p = 0.0216
	(Push duration) PV::hM4D CNO vs before	n = 8, 17	Mann-Whitney U-test	U = 30, p = 0.0011
	(%Resistance) PV::hM4D CNO vs before	n = 8, 15	Mann-Whitney U-test	U = 19, p = 0.006
	(%Retreat) PV::hM4D CNO vs before	n = 8, 15	Mann-Whitney U-test	U = 19, p = 0.006
2K	VIP::hM4D(CNO) vs VIP::hM4D(saline)	n = 6, 8	Two-way repeated measure ANOVA; Bonferroni multiple comparisons post hoc tests.	0.5h (p < 0.0001)；1.5h (p = 0.0003)；6h (p = 0.0046)

2L	(Push number) VIP::hM4D CNO vs before	n = 8, 19	Mann-Whitney U-test	U = 50, p = 0.1694
	(Push duration) VIP::hM4D CNO vs before	n = 8, 19	Mann-Whitney U-test	U = 28, p = 0.0091
	(%Resistance) VIP::hM4D CNO vs before	n = 8, 19	Mann-Whitney U-test	U = 11, p = 0.0002
	(%Retreat) VIP::hM4D CNO vs before	n = 8, 19	Mann-Whitney U-test	U = 11, p = 0.0002
4J	(change latency in push) PYR vs PV vs VIP	n = 30, 36, 27	Mann-Whitney U-test	VIP vs PYR: U = 231.5.5, p = 0.050; VIP vs PV: U = 235.5, p = 0.0004; PV vs PYR: U = 530, p = 0.9008
	(decay time in push) PYR vs PV vs VIP	n = 30, 36, 27	Mann-Whitney U-test	VIP vs PYR：U = 184.5, p = 0.0002; VIP vs PV: U = 219, p <0.0001; PV vs PYR: U = 500, p = 0.5781
4K	(change latency in retreat) PYR vs PV vs VIP	n = 27, 29, 32	Mann-Whitney U-test	VIP vs PYR: U = 353.5, p = 0.2358; VIP vs PV: U = 404.5, p = 0.3948; PV vs PYR: U = 287, p = 0.0874
	(decay time in retreat) PYR vs PV vs VIP	n = 27, 29, 32	Mann-Whitney U-test	VIP vs PYR: U = 391, p = 0.4911; VIP vs PV: U = 414.5, p = 0.4322; PV vs PYR: U = 390.5, p = 0.9886
5G	light on PV::tdTomato vs PV::JAWs neurons	n = 77, 154 (N = 3, 3)	Two-way repeated measure ANOVA	F (1.831, 283.8) = 4.919, p = 0.0098
5L	light on VIP::tdTomato vs VIP::JAWs neurons	n = 77, 123 (N = 2, 2)	Two-way repeated measure ANOVA	F (1.791, 218.5) = 6.242, p = 0.0033
6E	PV::Ai32 WS firing change Pre vs light on	n = 139, 139	Wilcoxon matched-pairs signed rank test	W = -9416, p < 0.0001
6F	PV::Ai32 NS firing change Pre vs light on	n = 39, 39	Wilcoxon matched-pairs signed rank test	W = -324, p = 0.023
6G	PV::Ai32 FSI firing change Pre vs light on	n = 16, 16	Wilcoxon matched-pairs signed rank test	W = 42, p = 0.2979
7K	VIP::Ai32 WS firing change Pre vs light on	n = 127, 127	Wilcoxon matched-pairs signed rank test	W = 5945, p < 0.0001
7L	VIP::Ai32 NS firing change Pre vs light on	n = 14, 14	Wilcoxon matched-pairs signed rank test	W = 94, p = 0.0015
7M	VIP::Ai32 FSI firing change Pre vs light on	n = 11, 11	Wilcoxon matched-pairs signed rank test	W = 42, p = 0.0645
S2B	PV::ChR2 OFT total distance light off vs light on	n = 8, 8	Paired t-test	t = 0.9066, df = 7, p = 0.3947
	PV::ChR2 OFT center duration light off vs light on	n = 8, 8	Paired t-test	t = 2.112, df = 7, p = 0.0725
S2C	VIP::ChR2 OFT total distance light off vs light on	n = 8, 8	Paired t-test	t = 0.5575, df = 7, p = 0.5946
	VIP::ChR2 OFT center duration light off vs light on	n = 8, 8	Paired t-test	t = 0.3781, df = 7, p = 0.7166
S7B	PV::JAWs non-PV neurons Area under curve change light off vs light on	n = 154, 154	Wilcoxon matched-pairs signed rank test	W = 2833, p = 0.0104
S7D	VIP::JAWs non-VIP neurons Area under curve change light off vs light on	n = 123, 123	Wilcoxon matched-pairs signed rank test	W = -2410, p = 0.0022

S11K	pPV-Inb vs pPyr-Act	n=7, 22	Kolmogorov-Smirnov two-sample test	p = 0.03
	pPV-Inb vs pPV-Act	n=7, 14	Kolmogorov-Smirnov two-sample test	p = 0.02
	pPV-Act vs pPyr-Act	n=14, 22	Kolmogorov-Smirnov two-sample test	p= 0.63
S12D	(change latency in push) PYR vs PV vs VIP vs SOM	n = 30, 36, 27, 30	Mann-Whitney U-test	VIP vs SOM: U = 186, p = 0.0003; SOM vs PV: U = 401.5, p = 0.0748;
	(decay time in push) PYR vs PV vs VIP vs SOM	n = 30, 36, 27, 30	Mann-Whitney U-test	VIP vs SOM: U = 206, p = 0.0011; SOM vs PV: U = 494, p = 0.5401;
S12E	(change latency in retreat) PYR vs PV vs VIP vs SOM	n = 27, 29, 32, 28	Mann-Whitney U-test	VIP vs SOM: U = 446, p = 0.9795; SOM vs PV: U = 354.5, p = 0.4161;
	(decay time in retreat) PYR vs PV vs VIP vs SOM	n = 27, 29, 32, 28	Mann-Whitney U-test	VIP vs SOM: U = 419, p = 0.6559; SOM vs PV: U = 335, p = 0.2232;